Final Report

CONTRACT NO: N00014-03-1-0028

DEVELOPMENT OF NOVEL PROCESS FOR THE DEPOSITION OF NANOSTRUCTURED TERNARY ALLOYS AND COMPOSITES FOR REPLACEMENT OF CADMIUM COATINGS

SUMBITTED TO:
DR. AIRAN PEREZ
OFFICE OF NAVAL RESEARCH,
ONR DEPARTMENT CODE 332
800 NORTH QUINCY ST.,
ARLINGTON, VA 22217

Submitted by:
Branko N. Popov
Center for Electrochemical Engineering
Department of Chemical Engineering
University of South Carolina
Columbia, SC 29208
Tel: (803) 777-7314
Fax: (803) 777-8265
E mail: popov@engr.sc.edu

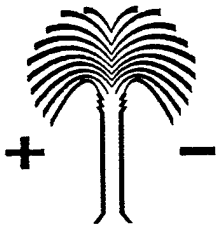

Center for Electrochemical Engineering
University of South Carolina
Columbia, SC 29208

December 2003

REPORT DOCUMENTATION PAGE			*Form Approved OMB No. 0704-0188*
Public reporting burden for this collection of information is estimated to average 1 hour per response, including the time for reviewing instruction, searching existing data sources, gathering and maintaining the data needed, and completing and reviewing the collection of information. Send comments regarding this burden estimate or any other aspect of this collection of information, including suggestions for reducing this burden, to Washington headquarters Services, Directorate for Information Operations and Reports, 1215 Jefferson Davis Highway, Suite 1204, Arlington, VA 22202-4302, and to the Office of Management and Budget, Paperwork Reduction Project (0704-0188) Washington DC 20503.			
1. AGENCY USE ONLY *(Leave blank)*	**2. REPORT DATE** December 2003	**3. REPORT TYPE AND DATES COVERED**	
4. TITLE AND SUBTITLE: Development of Novel Process for the Deposition of Nanostructured Ternary Alloys and Composites for Replacement of Cadmium Coatings			**5. FUNDING NUMBERS** N00014-03-1-0028
6. AUTHOR(S) Branko N. Popov			
7. PERFORMING ORGANIZATION NAME(S) AND ADDRESS(ES) Department of Chemical Engineering Swearingen Engineering Center University of South Carolina Columbia, SC 29208			**8. PERFORMING ORGANIZATION REPORT NUMBER**
9. SPONSORING / MONITORING AGENCY NAME(S) AND ADDRESS(ES) Office of Naval Research, 800 N. Quincy St., Arlington, VA 22217-5000			**10. SPONSORING / MONITORING AGENCY REPORT NUMBER**
11. SUPPLEMENTARY NOTES The views, opinions and/or findings contained in this report are those of the author(s) and should not be construed as an official Department of Army position, policy or decision, unless so designated by other documentation.			
12a. DISTRIBUTION / AVAILABILITY STATEMENT Approved for public release; distribution is unlimited.			**12b. DISTRIBUTION CODE**

13. ABSTRACT

The objective of this investigation was to develop novel processes for depositing ternary Zn-Ni-X (X=Cu or P) alloys for replacement of Cd coatings in sacrificial protection of steel substrates. Introducing small amounts of Cu in the Zn-Ni plating bath results in alloys with reduced amount of Zn in the final deposit. This alloy shows improved corrosion performance that is 4 times higher than that of Cd coatings. Also, the use of autocatalytic method was investigated to deposit amorphous Ni-Zn-P alloys. The electroless Ni-Zn-P alloy shows improved corrosion performance that is 5 times higher than that of Cd coatings and reduces the hydrogen ingress into steel to 94%. A novel electrolytic process was developed to deposit Ni-Zn alloys with high Ni content. Deposition parameters like pH and temperature were optimized based on composition and the surface morphology of the coating. The Zn content in the coating was optimized based on the corrosion resistance of the final deposit. Finally, corrosion studies shows that Ni-Zn coatings obtained using these methods show a 5 times increase in barrier resistance as compared to Cd coatings. Also a mathematical model was developed to study the electroless Ni-Zn-P deposition.

14. SUBJECT TERMS Steel, Zn-Ni alloys, Sacrificial Protection, Corrosion resistance, Hydrogen Embrittlement, electroless process, model.			**15. NUMBER OF PAGES** 80
			16. PRICE CODE
17. SECURITY CLASSIFICATION OF REPORT Unclassified	**18. SECURITY CLASSIFICATION OF THIS PAGE** Unclassified	**19. SECURITY CLASSIFICATION OF ABSTRACT** Unclassified	**20. LIMITATION OF ABSTRACT** UL

PREFACE

This final report describes the research work performed under the Office of Naval Research (ONR) grant number N00014-03-1-028. This work is a continuation of our studies into the development of novel ternary alloys and composites for preventing the corrosion and hydrogen embrittlement of steel substrates. Specifically, these alloys are developed to replace cadmium coatings used in naval applications such as landing gears for aircrafts used in naval warfare. This research work was completed as part of the Ph. D. degree studies of Kim Hansung, Basker Veeraraghavan and Swaminatha Prabu Kumaraguru in the Department of Chemical Engineering at the University of South Carolina. Kim Hansung completed his Ph. D. studies in August 2003 and Basker Veeraraghavan in November 2003. The following papers were either published or are being prepared for publication in technical journals based on this research:

1. Basker Veeraraghavan, Bala Haran and Branko Popov, *"Study of Electroless Ni-Zn-P Deposition Process"* Submitted to *Electrochim. Acta*
2. Basker Veeraraghavan, Hansung Kim, Bala Haran and Branko Popov, *"Comparison of Mechanical, Corrosion and Hydrogen Permeation Properties of Electroless Ni-Zn-P Alloys with Electrolytic Zn-Ni and Cd Coatings"* accepted for publication in *Corrosion.*
3. Swaminatha P Kumaraguru, Basker Veeraraghavan and Branko N. Popov , *"Novel Plating Process for the Deposition of Zn-Ni-Cu as a Replacement for Cadmium Coatings,"* Submitted to *J.Electrochem. Soc.*
4. Swaminatha P Kumaraguru, Basker Veeraraghavan and Branko N. Popov , *"Non-Aanomalous Ni-Zn alloys for the Corrosion Protection of Steel"*, Under review

The research described in this report includes the deposition of novel ternary Zn-Ni-Cu alloy to inhibit corrosion and hydrogen embrittlement of steel substrates. Also a mathematical model to study the electroless Ni-Zn-P has been described. Further study includes the development of an electrolytic process deposit high Ni-Zn alloys. The use of these alloys holds promise in replacing cadmium as they may provide enhanced hydrogen permeation inhibition while simultaneously protecting the steel against galvanic corrosion.

TABLE OF CONTENTS

PREFACE.....2

TABLE OF CONTENTS.....3

LIST OF TABLES.....4

LIST OF FIGURES.....5

LIST OF SYMBOLS.....8

EXECUTIVE SUMMARY.....10

RESULTS AND DISCUSSION.....12

1. INTRODUCTION.....12
2. EXPERIMENTAL.....17
3. DISCUSSIONS.....20
4. CONCLUSIONS.....44
5. REFERENCES.....47
6. APPENDIX.....51
7. TABLES.....52
8. FIGURES.....55

LIST OF TABLES

Table 1 Experimental Conditions used in the study.....52

Table 2 Kinetic Parameters used in the model.....52

Table 3 Variation in Corrosion potential and Corrosion current density as a function of Zn content in the coatings.....53

Table 4 Corrosion properties of different sacrificial coatings determined by linear and tafel polarization studies.....53

Table 5 Comparison of mechanical properties for the various sacrificial coatings.....54

Table 6 Kinetic parameters characterizing the hydrogen evolution and permeation through various coatings.....54

LIST OF FIGURES

Figure 1 Variation in equilibrium concentrations of complexed Zn and Ni species as a function of bath pH.....55

Figure 2 Polarization studies of hypophosphite oxidation on different substrates.....55

Figure 3 Dimensionless concentration profiles for the various reactants as a function of distance from the electrode surface.....56

Figure 4 Evans diagram showing the various reactions happening during the electroless deposition process for a $ZnSO_4$ concentration of 5 g/L.....56

Figure 5 Comparison of mixed potential E_m and plating current density i_{pl} obtained from the model and the experiments as a function of $ZnSO_4$ concentration in the bath.. 57

Figure 6 Linear polarization studies performed during the deposition process as a function of $ZnSO_4$ concentration in the bath.....57

Figure 7 Variation in Surface Coverages of the different reacting species as a function of $ZnSO_4$ concentration in the bath.....58

Figure 8 Variation in Ni content as a function of $ZnSO_4$ concentration in the bath.....58

Figure 9 Variation in Zn and P content as a function of $ZnSO_4$ concentration in the bath.....59

Figure 10a Comparison of mixed potential E_m and plating current density i_{pl} obtained from the model and the experiments as a function of pH of the bath.....59

Figure 10b Variation in Surface Coverages of the reacting species as a function of bath pH.....60

Figure 11 Comparison of Ni, Zn and P contents of the coating obtained from the model and the experiments as a function of pH of the bath.....60

Figure 12 Variation in the composition of the coatings obtained as a function of $ZnSO_4.7H_2O$ concentration in the bath.....61

Figure 13a Cathodic Polarization curves obtained from for the alkaline bath, in the absence of $NiSO_4.6H_2O$ and $ZnSO_4.7H_2O$ an in the presence of $ZnSO_4.7H_2O$.....61

Figure 13b Cathodic polarization curves obtained from an alkaline the presence and absence of $ZnSO_4.7H_2O$.....62

Figure 14 Partial current density of Ni and Zn in alloy and single metal deposition as a function of applied potential.....62

Figure 15 Variation in composition and thickness of the deposit as a function of the applied potential.....63

Figure 16 SEM Micrographs of N-Zn alloy deposited at (a) -1.0 V, (b)-1.1 V, (c) -1.3 V and (d) -1.5 V. 63

Figure 17 Tafel analysis of the Ni-Zn coatings as a function of Zn content in the final deposit. The corrosion potential becomes more electronegative as more Zn is included in the deposit.....64

Figure 18 Variation in composition of the deposit as a function of the pH of the bath.....64

Figure 19 Variation in the composition of the deposit as a function of bath temperature.....65

Figure 20 Variation in the deposition rate as a function of the bath temperature.....65

Figure 21 EDAX analysis of Zn-Ni alloy (88-12 %) and Zn-Ni-Cu alloy (45-35-20%).....66

Figure 22 Cyclic voltammogram of Zn-Ni-Cu film electrodeposited from a solution of 40 g/L of NiSO4.6H2O, 20 g/L of ZnSO4 and 1 g/L of CuSO4 at a scan rate of 30 mV/s. 66

Figure 23 Effect of $CuSO_4$ concentration on the alloy composition of electrodeposited Zn-Ni-Cu as a function of applied (negative) potential. 67

Figure 24 Effect of $CuSO_4$ concentration on the partial current density of electrodeposited Zn-Ni-Cu as a function of applied (negative) potential. 68

Figure 25 Effect of stirring on the composition of Zn-Ni-Cu alloy electrodeposited from 60 g/L of $NiSO_4.6H_2O$, 30 g/L of $ZnSO_4.7H_2O$ and 1 g/L of $CuSO_4$, pH 9.0 at -1.3 V (vs. SCE). 69

Figure 26 Effect of $ZnSO_4.7H_2O$ concentration on the composition of the Zn-Ni-Cu alloy electrodeposited from 60 g/L of $NiSO_4.6H_2O$, ZnSO4.7H2O in the presence of a) 1 g/L of $CuSO_4$, and b) 2 g/L of $CuSO_4$ pH 9.0 at -1.3 V (vs. SCE).....70

Figure 27 Effect of ZnSO4 concentration and additive on the current density of deposition as a function of time.....71

Figure 28 Surface morphology of the coatings at the three points indicated in Figure 27... 72

Figure 29 SEM micrograph of Zn-Ni-Cu deposit obtained from the bath containing additives, 0.5 g/L dextrin, and 60g/L of sodium citrate.....73

Figure 30a: Linear polarization plots for the various sacrificial coatings as compared with optimized Ni-Zn (28-wt% Zn) and Ni-Zn-P coatings. The graph shows a four-times increase in the polarization resistance for these coating as compared to Cd coating.....73

Figure 30b Comparison of corrosion rates of various alloy coatings.....74

Figure 31 Nyquist plots obtained for various coatings in 71 g/L Na_2SO_4 and 30.5 g/L H_3BO_3 (pH=7.0) solution.....74

Figure 32 E_{orr} vs. time plot for the various alloy coatings (thickness=2 μm) immersed in 71 g/L Na_2SO_4 and 30.5 g/L H_3BO_3 (pH=7.0) 75

Figure 33 Hydrogen permeation current transients through Ni-Zn-P deposit as a function of time for different applied cathodic potentials. 76

Figure 34 Variation of cathodic current densities (i_c) as a function of applied overpotential (η) for Ni-Zn-P and Zn-Ni deposits. 76

Figure 35 Variation of hydrogen permeation current densities (i_a) as a function of applied overpotential (η) for Ni-Zn-P and Zn-Ni deposits. 77

Figure 36 The hydrogen entry efficiency (i_a/i_c x 100) as a function of overpotential (η) for Zn-Ni, Ni-Zn-P and Cd coatings. 77

Figure 37 Plot of hydrogen permeation current (i_a) vs. square root of the recombination current ($\sqrt{i_r}$) for Ni-Zn-P and Zn-Ni coatings. 78

Figure 38 Plot of hydrogen charging function ($i_c e^{a\alpha\eta}$) vs. steady state hydrogen permeation current (i_a) for Ni-Zn-P and Zn-Ni coating. 78

Figure 39 Dependence of surface hydrogen coverage (θ_s) on the hydrogen overpotential (η for Ni-Zn-P, and Zn-Ni coatings. 79

LIST OF SYMBOLS

b_j	Concentration dependant adsorption co-efficient for species j, cm^3/mol
$C_{s,j}$	Surface concentration of species j, mol/cm^3
$C_{b,j}$	Bulk concentration of species j, mol/cm^3
D_j	Diffusion coefficient for species j, cm^2/s
$E_{0,j}$	Standard-state potential for reaction j, V
$E_{eq,j}$	Equilibrium potential for reaction j, V
E_m	Mixed potential for the electroless deposition process, V
F	Faraday's constant, 96487 C/(g.eq)
K_j	Stability constant for the complexed species j, dimensionless
i_j	Current density for reaction j involved in the deposition process, A/cm^2
$i_{0,j}$	Equilibrium exchange current density for reaction j, A/cm^2
i_{pl}	Plating current density for the deposition process, A/cm^2
M_j	Molecular weight of species j, g/mol
R_p	Polarization resistance measured during the electroless deposition process, Ω-cm^2
m_j	Mass of component j in the deposit, g
n_j	Number of electrons for species j involved in the electrode reaction
R	Gas constant, 8.314 J/(gmol-K)
s_{ij}	Stoichiometric co-efficient for species j involved in reaction i, dimensionless
t	Time of deposition process, s
T	Absolute temperature, K
x	Normal distance from the electrode, cm
a	a constant, F/RT, V^{-1}
b	a constant, L/FD, $mol.(A.cm)^{-1}$
C_s	Absorbed hydrogen concentration
D	hydrogen diffusion coefficient, $cm^2.s^{-1}$
F	Faraday's constant, 96487 $C.(g.eq)^{-1}$
i_c	hydrogen charging current density, $A.cm^{-2}$

i_a steady state permeation flux, $A.cm^{-2}$

i_r steady state recombination flux ($=i_c - i_a$), $A.cm^{-2}$

i_0 modified exchange current density, $A.cm^2$

k_1 discharge reaction rate coefficient, $mol.(cm^2.s)^{-1}$

k_3 recombination rate constant, $mol.(cm^2.s)^{-1}$

k_{abs} absorption rate constant, $mol.(cm^2.s)^{-1}$

k_{ads} adsorption rate constant, $cm.s^{-1}$

$k^{"}$ Thickness dependent absorption-adsorption rate constant, $mol.cm^{-3}$

L membrane thickness, cm

R gas constant, 8.314 $J.(gmol.K)^{-1}$

T temperature, K

Greek symbols

α_j Anodic transfer co-efficient for species j involved in the reaction

β_j Cathodic transfer co-efficient for species j involved in the reaction

δ_j Thickness of Nernst stagnant diffusion layer, cm

η_j Surface overpotential for reaction j, V

ω Rotation speed for the disk electrode, rad/s

υ Kinematic viscosity of the electrolyte, cm^2/s

θ_j Surface coverage for species j involved in the electrode reaction, dimensionless

α Transfer coefficient, dimensionless

η Overvoltage, V

θ_s surface hydrogen coverage, dimensionless

EXECUTIVE SUMMARY

A mathematical model based on mixed potential theory has been developed to explain the reactions happening during electroless Ni-Zn-P deposition process. The mathematical model was developed by assuming an adsorption step in the reaction mechanism in addition to the electrochemical step. Based on the model, it was seen that adsorption plays a significant role in the deposition process. It was also seen that addition of Zn ions to the bath inhibits the deposition process by changing the surface coverages for the adsorbed reactants on the electrode surface. This inhibition effect was also experimentally analyzed by studying the effect of Zn ions on polarization resistance of the deposition process. The composition of the coating was predicted from the model by obtaining the partial current densities for Ni, Zn and P deposition reactions. The effect of pH on the deposition process was also studied using the model. The results obtained from the model agree well with the experimental observations, confirming the mechanism assumed in the mathematical model.

In addition to the corrosion and engineering properties of the Ni-Zn-P alloys, hydrogen permeation characteristics of the electroless Ni-Zn-P alloy was studied and compared with that of Cd and Zn-Ni coatings. The exchange current density, i_0; thickness dependent adsorption-absorption rate constant, k^*; recombination rate constant, k_3; and the surface hydrogen coverage, θ_S that characterize the hydrogen evolution kinetics of the coatings were obtained by applying a mathematical model to experimental results. From the resulting data analysis, Ni-Zn-P alloy was seen not only to provide longer life under corroding media, but also reduces greatly the risk of the substrate being exposed to hydrogen embrittlement when compared to electrodeposited Cd and Zn-Ni coatings. Apart from replacing these two coatings, Ni-Zn-P coatings can also be used under cathodic protection due to their low hydrogen permeation characteristics.

Further studies were performed to replicate the electroless Ni-Zn-P by an electrolytic process. A novel electrolytic method for obtaining non-anomalous Ni-Zn coatings with high Ni content (72-wt% as compared to 15-20 wt% in conventional Zn-Ni deposition) has been developed. Ni-Zn coatings were cathodically deposited from alkaline sulfate electrolytes in the presence of complexing agents and additives. The Zn content in the coating was optimized based on the corrosion resistance and corrosion potential of the final deposit. The higher amount of

nickel content in the deposit induces barrier properties and the presence of zinc helps to maintain the sacrificial nature of the coating. Corrosion potential of the optimized Ni-Zn alloy was –0.678 V vs. SCE. This low potential is a result of the decreased Zn content in the deposit. Deposition parameters such as applied potential and pH have been optimized based on composition of the coating and the surface morphology. Corrosion studies show that Ni-Zn coatings obtained using this method show a higher barrier resistance and better stability as compared to Cadmium coatings

In order to obtain a composite ternary Zn-Ni alloy with out cadmium, a novel plating process for the electrodeposition of Zn-Ni-Cu was developed. The inclusion of the ternary alloying element copper into the deposit decreases the Zn:Ni ratio with simultaneous increase in the nickel content. An effective method to control the Zn:Ni ratio has been optimized. It has been shown that use of 1 g/L of $CuSO_4$ in the Zn-Ni bath leads to copper codeposition along with Zn and Ni. The Zn-Ni alloy deposit is enriched with a high content of nickel and the Zn:Ni ratio is lowered to 1.3:1. Corrosion resistant Zn-Ni-Cu alloy of composition Zn – 45%, Ni - 35% and Cu-20% was obtained. The corrosion characteristics of the Zn-Ni-Cu coating showed a five times increase in the corrosion resistance in comparison with conventional Zn-Ni alloys. The corrosion potential of the Zn-Ni-Cu alloy obtained was –0.69 V vs SCE. This low potential is a result of the decreased Zn content in the deposit. Owing to its high barrier resistance and superior corrosion properties, Zn-Ni-Cu alloy is proposed as an ideal replacement for cadmium coatings

.

1. INTRODUCTION

Steel substrates are electrodeposited with sacrificial coatings for corrosion protection. Zn, Zn-Ni, Zn-Co and Cadmium alloys are some of the widely used sacrificial coatings [1-8]. Among them cadmium coatings are considered very reliable owing to their superior corrosion and engineering properties [2]. However, the cadmium coatings are highly toxic and they are generally prepared from toxic cyanide baths [3]. Also cadmium plating introduces large amount of hydrogen in the underlying substrate, thus increasing the susceptibility of the substrate to hydrogen embrittlement [4]. Growing ecological concerns in recent years have led to the search for an alternative coating that can effectively replace cadmium. Zinc deposits exhibit excellent sacrificial behavior. However, a high dissolution rate and poor mechanical properties limit the use of Zn coatings in the automotive industry. Alloying of zinc with noble metals like nickel has proved to increase the corrosion resistance and mechanical properties of zinc coatings. Zn-Ni alloys are considered as a viable alternative to cadmium coatings [6-11]. Zn-Ni alloys containing 15 - 20 wt% of nickel possess four times more corrosion resistance than cadmium-titanium coatings [12]. Although zinc is less noble than nickel, the electrodeposition of Zn-Ni results in the preferential deposition of the zinc and a higher amount of zinc is observed in the final deposit. Therefore, Brenner classifies Zn-Ni codeposition as anomalous [13]. The mechanism for the preferential deposition of Zn has been discussed extensively in literature [13,14]. Due to the higher percent of zinc in the coating, these alloys are more electronegative than cadmium and hence dissolve rapidly in corrosive environments. Any further increase in nickel composition is based on using a higher than predicted Ni/Zn ratio in the bath [15,16]. Though Zn-Ni alloys have good corrosion resistance in comparison with Zn coating, further development for better coating and corrosion characteristics is of commercial interest. An enhancement in the nickel composition of these alloys would lead to more anodic open circuit potential, which will in turn reduce the driving force for galvanic corrosion. Also the barrier properties of the coating increases with increased nickel content in the deposit. Several attempts have been made earlier to decrease the anomaly and increase the nickel content by either introducing an inert species in the bath or by developing a ternary alloy [17-24]. Nonyl phenyl polyethylene oxide (NPPO) has been used to reduce the Zn-Ni ratio and produce more corrosion resistant deposits. NPPO inhibited zinc electrodeposition and acted as a leveling agent as seen in our earlier studies on the

deposition of zinc and galvanostatic pulse and pulse reversal plating of Zn-Ni alloys from sulfate electrolytes[20,21].

Codeposition of phosphorous along with Zn-Ni alloy improves the corrosion resistance [17] and hydrogen permeation [18] characteristics of the deposit. Zhou et al [19] have studied the effect of tin additions on the anomalous deposition behavior of Zn-Ni alloys. The nickel ratio increased from 6 to 8 % with the addition of small amounts of tin. Earlier, we have developed a novel plating process for the electrodeposition of Zn-Ni-Cd coatings [22-24]. It was found that use of small of ternary alloying elements like cadmium can effectively control the Zn-Ni ratio. Cadmium codeposition was observed with a significant decrease in the Zn-Ni ratio. The Zn-Ni ratio [24] was as low as 1.7:1. Also the corrosion resistance of the coating was improved by an order of magnitude when compared to that of commercial Zn-Ni and cadmium coatings. The inclusion of ternary element like cadmium prevented the hydrogen entry in to the substrate as compared to the Zn-Ni alloy and cadmium coatings [23]. However, the trace of cadmium present in the bath poses ecological concerns. Hence the objective of the present study is to develop cadmium free coatings that can effectively replace cadmium. The goal of the present study is to develop a unique plating process for the deposition of Zn-Ni-Cu ternary alloys, which will induce barrier properties to the sacrificial Zn-Ni alloy and increase the life of the coating. An increase in the nickel content of the deposit with a simultaneous decrease in the Zn:Ni ratio is expected on alloying with the ternary element copper. This leads to a decrease in the sacrificial potential, which is the primary driving force for the faster dissolution of Zn-Ni alloy.

Autocatalytic reduction of metals and alloys offers an attractive and alternate method of increasing the amount of Ni in the final deposit. Electroless deposition has been used to form a thin and uniform Ni-Zn -P film from both sulfate and chloride baths. Previous efforts have shown that Ni-Zn-P plating follows normal deposition with high Ni content (85-90%) and excellent corrosion properties [25-27]. However, in these cases, the amount of Zn remains low (~10 wt%) and hence the potential (-476 mV vs. SCE) is more positive to steel (-590 mV vs. SCE). Thus these deposits could not be used as a sacrificial coating to protect steel. Previously, we have developed Ni-Zn-P alloys from an alkaline electrolyte with optimum amount of Zn content that offers sacrificial protection to steel substrates [28]. The corrosion and hydrogen permeation characteristics of these newly developed composite coatings were compared with that of

cadmium [29]. These studies showed that the developed Ni-Zn-P alloys exhibit better corrosion and hydrogen permeation properties than Cd. The inclusion of Zn in the final deposit has been studies by several authors [25-27]. However, the mechanism of deposition has not been explored in detail [25-27]. In the present study a model based on mixed potential theory has been used to elucidate the Ni-Zn-P deposition process.

Mixed potential theory was used initially by Paunovic [30] and then by Donohue [31] to explain the electroless deposition processes. According to the mixed potential theory, the electroless plating process occurs due to a combination of the oxidation and reduction reactions, the rates of which are equal and opposite at any given time of deposition. Bindra and Roldan [32], and then Ohno *et. al.* [33] have done electrochemical studies on electroless deposition processes and reported that the reactions occurring during an electroless process can be explained by an electrochemical mechanism. Ramasubramanian *et. al.* also showed that electroless deposition of copper from a formaldehyde bath can be explained using mixed potential theory [34]. For the case of nickel electroless deposition, the mechanism is not clearly understood and still debatable. Abrantes and Correia proposed a mechanism based on adsorption of hypophosphite and subsequent electrochemical reduction of Ni for explaining the electroless deposition of Ni-P alloys [35]. However, Paunovic and Schlesinger have shown that the electroless deposition of nickel in the presence of DMAB can be explained by mixed potential theory [36]. Kim and Sohn explained the electroless deposition of Ni-P from an acidic bath on a rotating disk electrode with the help of a mathematical model based on mixed potential theory [37]. In general, the electrochemical mechanism has been favored for explaining the electroless deposition processes. In this study, a mathematical model based on mixed potential theory was developed to explain the reactions occurring at steady state on a rotating disk electrode surface.

On the other hand, Ni-Zn alloys with increased nickel content in the deposit were developed by an electrolytic process. It has been previously observed [38] that Zn is co-deposited during potentiostatic deposition from a Zn-Ni bath in the potential range –0.7 to –0.9 V *vs.* Ag/AgCl. This produces a non-anomalous coating with 70-wt% Ni. [16]. However, the deposits have high stresses and poor adhesion in such cases and cannot be used as protective coatings. In this study, a novel plating process was developed for deposition of Ni-Zn composites from an alkaline bath with high Ni content. In other words, the second part of this study is focused on

developing non-anomalous Ni-Zn coatings which provide sacrificial protection to steel and have low dissolution rates. The corrosion characteristics of these newly developed composite coatings were estimated using standard electrochemical techniques and were compared to those of cadmium.

Several techniques have been used to decrease the problem of hydrogen embrittlement of steel. These include post-treatment annealing, laser surface modification and shot preening [46-49]. These methods however, do not decrease the hydrogen entry below a safe level that can prevent cracking hazards. On the other hand, electroplating of the substrate with a suitable metal/alloy coating holds promise in reducing the hydrogen influx into the metal [50]. However, the necessary prerequisite for such coatings is that they should have the intrinsic capability of providing sacrificial protection should the substrate be exposed. Jin-Ming Chen and Jiann-Kuo Wu [51] reported the effect of copper, tin, silver and nickel-plating on hydrogen permeation inhibition in AISI 4140 steel. It was found that copper and tin effectively reduced the hydrogen permeation by over 80%. However, the corrosion resistance behavior was not presented for these electrodeposited metals and comparing the standard potentials of these alloys reveals that should the substrate become exposed, the substrate instead of the coating would corrode. Cadmium plating has been extensively used as a corrosion resistant coating on hard steel for various applications [50]. Zamanzadeh *et al.* found that deposits of cadmium reduced the hydrogen adsorption on iron [52]. In a report of our latest work, we had presented results on a novel electroless process that gave rise to the deposition of high Ni content (74-wt%) Ni-Zn-P alloys that can be applied as a sacrificial coating for steel substrates. The developed Ni-Zn-P alloys possess excellent corrosion properties as compared to Cd coatings. The objective of this work is to determine the hydrogen permeation properties of the Ni-Zn-P deposits and compare it with that of Zn-Ni and Cd deposits obtained from commercial baths. Several models have tried to explain hydrogen entry into metal substrates and to evaluate kinetic parameters of hydrogen evolution and permeation based on experimental data [53-58]. The most significant of them is the model proposed by Iyer *et al.* [56]. However, an important assumption used in this model is the low hydrogen coverage, and cannot be applied when the hydrogen coverage is high. The basic IPZ model was then modified by Iyer *et al.* [57] to accommodate high hydrogen surface coverage and in this paper, this modified model has been used to analyze the experimental results during

instances of increased surface coverage. The effect of various kinetic parameters of hydrogen evolution on the permeation current density under various degrees of cathodic polarization was predicted from the analysis.

2. EXPERIMENTAL

Sample Preparation:- Plating and subsequent corrosion studies were done on low carbon cold-rolled steel foils with thickness of 0.5 mm and area of 25 x 25 mm. Initially, the steel sample was mechanically polished with successive finer grades of emery paper. The samples were then degreased with alcohol and rinsed with de-ionized water. Next, the samples were treated in 10 % (v/v) H_2SO_4 solution for 1 minute to remove any adherent oxide layer present on the surface. *Electroless deposition of Ni-Zn-P:-* Ni-Zn-P composites were prepared from a bath containing 35 g/L $NiSO_4$ in the presence of complexing agents. Sodium hypophosphite was used as a reducing agent for the auto-catalytic process and as a source of P in the final deposit. The depositions were carried out in alkaline electrolytes. Ni-Zn-P coatings with different amounts of Zn were obtained by varying the amount of $ZnSO_4.7H_2O$ in the bath. The deposition temperature was maintained at 85±1 °C using a double-jacketed vessel with a temperature controller. The deposition time was kept constant. . The pH was maintained at 10.5 during the deposition process by addition of sodium hydroxide. All solutions were prepared with analytical grade reagents (obtained from Sigma-Aldrich) and distilled water. The experimental conditions are given in Table 1. A steel rotating disk electrode was used as the working electrode, while a platinum wire served as a counter electrode. A standard calomel electrode (SCE) was used as a reference electrode. In the model, appropriate corrections were made for the potential of the SCE with respect to the temperature of the deposition process (E_{SCE} at 85 °C = -0.195 V vs. NHE). The mixed potential for the deposition was then measured using a standard calomel electrode (SCE). Linear polarization studies during the deposition process were obtained by scanning the potential 10 mV above and below the deposition potential after initiating the deposition process.

Electrolytic Ni-Zn process: Ni-Zn composites were prepared from a bath of alkaline sulfate electrolytes similar to the bath used in our electroless process [28]. Complexing agents were used to prevent Ni and Zn from precipitating. Steel foil was used as the substrate. Ni-Zn coatings with different amounts of Zn were obtained by varying the applied potential and also by varying the amount of $ZnSO_4.7H_2O$ in the bath. The deposition was carried out at 60 °C unless otherwise mentioned. The pH was maintained at 10.5 during the deposition and was maintained by addition of NaOH. The deposition time was changed according to the required thickness of the coating.

Ternary Zn-Ni-Cu alloy deposition: Preliminary studies were performed from an electrolytic bath of 60g/L $NiSO_4.6H_2O$, 30 g/L $ZnSO_4.7H_2O$ and $CuSO_4$. The amount of $CuSO_4$ is varied to control the Zn:Ni ratio as desired. Complexing agents and additives were used to further improve the properties of the deposit. The samples were electrodeposited potentiostatically using an EG&G PAR model 273 potentiostat interfaced with a computer. A three-electrode setup in a jacketed cell was used to plate the deposits. The steel foils prepared as described above were used as the working electrode. Platinum foil of equal area to that of the working electrode was used as a counter electrode and a standard calomel electrode (SCE) was used as a reference electrode. The distance between the working and counter electrode was maintained at a constant value of 1.5 cm. The deposition time was changed according to the required thickness of the coating. All solutions were prepared with analytical-grade reagents and triply distilled water.

Material Characterization:- Energy Dispersive Analysis using X-rays (EDAX) was used to analyze the distribution of the elements in the final deposit. To ensure accuracy of the element distributions, EDAX analysis was done at several points on the surface of the substrate. The accuracy of the measurements for the equipment used was rated as ±0.1-wt%. The surface morphology and the microstructure of the coating were analyzed using Scanning Electron Microscopy with the help of Hitachi S-2500 Delta Scanning Electron microscope. The thickness of the specimens was measured using cross-sectional SEM analysis.

Electrochemical Characterization:- A variety of electrochemical techniques including Linear and Tafel polarization were used to evaluate the barrier resistance properties of the coating. Since chemical dissolution of Zn occurs in both acidic and alkaline media, the electrochemical characterizations were carried out in a bath containing 0.5M Na_2SO_4 and 0.5M H_3BO_3 at pH 7.0. The electrochemical characterization was done using an EG&G PAR model 273A potentiostat/galvanostat interfaced with a computer and a three-electrode setup. The steel substrate with the coating was used as the working electrode and a platinum mesh was used as the counter electrode. A standard calomel electrode (SCE) was used as the reference electrode.

Hydrogen Permeation Characterization:- For the hydrogen permeation studies, one side of the steel membrane is coated with the alloy being tested and the other side of the steel membrane was electrodeposited with a thin layer (0.15~0.2 μm) of palladium to avoid corrosion reactions on steel that might perturb the permeation analysis. Pd deposition was carried out using 1×10^{-4} M

potassium tetranitropalladate ($K_2Pd(NO_2)_4$) at a current density of 200 $\mu A/cm^2$ for two hours. To ensure uniformity in testing, the thickness of all deposits tested was kept the same (2 μm for Ni-Zn-P/Cd/Zn-Ni and 0.2 μm for Pd). The prepared membrane samples were then fitted into the Devanathan - Stachurski permeation cell [59]. This cell setup consists of two working compartments, cathodic and anodic chamber, and the membrane is placed between two chambers. The palladium-plated side faces the anodic side and the side with the deposit faces the cathodic side. Permeation studies were performed using EG&G PAR model 273 potentiostat connected to each side. Platinum mesh was used as the counter electrode in each side and the membrane was used as a bipolar working electrode. Standard calomel (SCE, with a standard potential of 0.28 V *vs.* SHE) and mercuric oxide (Hg-HgO, with a standard potential of 0.926 V *vs.* SHE) reference electrodes were used for the cathodic and anodic sides respectively. The anodic compartment was filled with 0.2 M of NaOH solution and potential was kept at –0.3 V *vs.* Hg/HgO reference electrode until the background current falls below 0.5 $\mu A/cm^2$. This value corresponds to a practically zero concentration of atomic absorbed hydrogen on the surface. Then, the cathodic compartment was filled with a supporting electrolyte containing 0.5 M Na_2SO_4 + 0.5 M H_3BO_3 solution at pH 7.0. Nitrogen was purged on both sides throughout the experiment in order to remove dissolved oxygen from the electrolytes. The membrane on the cathodic side of the cell was polarized potentiostatically, creating conditions for hydrogen evolution. Hydrogen generated on the cathodic side permeates through the membrane and gets oxidized on the anodic surface of the membrane. The steady state currents associated with anodic (permeation current) and cathodic (charging current) reactions were monitored continuously by changing the overpotential for hydrogen evolution reaction at the cathodic side.

3. DISCUSSION

Part 1. Study of Electroless Ni-Zn-P deposition:-

Model Development:

In order to understand the processes occurring during the electroless Ni-Zn-P deposition process from alkaline electrolytes and to optimize the process a first principles mathematical model was developed. The reactions which were considered in the model are:

Oxidation of Hypophosphite [37, 39]

$$H_2PO_2^- + H_2O \xrightarrow{\text{Catalytic surface}} H_2PO_3^- + 2H^+ + 2e^- \quad (1)$$

Reduction reaction for P [37, 39]

$$2H_2PO_2^- + H^+ + e^- \rightarrow P + HPO_3^{2-} + H_2O + H_2 \quad (2)$$

Reduction reaction for Ni [39]

$$Ni(NH_3)_6^{2+} + 2e^- \rightarrow Ni + 6NH_3 \quad (3)$$

Reduction reaction for Zn [39]

$$Zn(NH_3)_4^{2+} + 2e^- \rightarrow Zn + 4NH_3 \quad (4)$$

H_2 evolution reaction [37, 39]

$$2H^+ + 2e^- \rightarrow H_2 \quad (5)$$

Concentration Profile in the Diffusion Layer

Concentration profiles for each of the reacting species in the deposition process of Ni-Zn-P alloys on a rotating disk electrode are described by the steady-state diffusion equation, expressed as

$$D_j \frac{\partial^2 C_j}{\partial x^2} = 0 \quad (6)$$

The boundary condition for the diffusion equation is given by

$$-D_j \frac{\partial C_j}{\partial x} = \sum_{i=1}^{n} \frac{s_{ji} i_j}{n_j F} \qquad \text{at x=0} \quad (7)$$

where n is the number of reactions occurring at the electrode surface in which the reacting species are involved. The stoichiometric co-efficient s_{ji} for each species j of reaction i is found out by:

$$\sum_i s_{ij} M_i \rightarrow n_j e^- \qquad (8)$$

where M_i is the species involved in each of the reaction

$$C_j = C_{b,j} \qquad \text{at } x=\delta \qquad (9)$$

where $C_{b,j}$ is the concentration of the species at the bulk of the electrolyte. The diffusion layer thickness δ for each of the species is defined by the relation

$$\delta_j = 1.61 D_j^{1/3} \omega^{-1/2} \upsilon^{1/6} \qquad (10)$$

where D_j is the diffusion co-efficient of the species, ω is the angular velocity of the rotating disk electrode and υ is the kinematic viscosity of the electrolyte.

Adsorption of Species at the Electrode Surface

At the electrode surface, the reacting species are adsorbed on the surface according to the following reactions

$$H_2PO_{2,s}^- \rightleftarrows H_2PO_{2,ad}^- \qquad (11)$$

$$Zn(NH_3)_{4,s}^{2+} \rightleftarrows Zn(NH_3)_{4,ad}^{2+} \qquad (12)$$

$$Ni(NH_3)_{6,s}^{2+} \rightleftarrows Ni(NH_3)_{6,ad}^{2+} \qquad (13)$$

$$H^+_{,s} \rightleftarrows H^+_{,ad} \qquad (14)$$

The surface coverage for each species follows an equilibrium isotherm of the form

$$\theta_j = \frac{b_j C_{s,j}}{1 + b_j C_{s,j}} \qquad (15)$$

where b_j is the concentration dependant adsorption co-efficient for each of the reacting species. The empirical relations for the dependence of b_j on concentration of all electroactive species were obtained by fitting the experimental results to the model. A similar approach for the adsorption phenomenon has been used by Wasberg and Horanyi to study the inhibition effects of chloride ions on reduction of nitric acid reduction on rhodium electrodes [40].

The surface coverages were also governed by the condition

$$\sum \theta_j = 1 \tag{16}$$

It is assumed that desorption of products from the electrode surface is fast enough that at any given time during the deposition process, the electrode surface is covered only by the reacting species.

Application of Mixed Potential Theory:

According to mixed potential theory, the electroless process occurs at a potential where the net current is zero. At this potential the current due to the anodic reaction (oxidation of hypophosphite) equals the sum of the cathodic currents (reduction of Ni, Zn, P and H_2). The following condition gives the relationship between the various partial current densities

$$i_1 = |i_2| + |i_3| + |i_4| + |i_5| \tag{17}$$

where i_1 is the current density due to oxidation of hypophosphite, i_2 represents the partial current density for P reduction, i_3 is the partial current density of Ni reduction, i_4 corresponds to the partial current density of Zn reduction and i_5 is the partial current density due to H_2.

Assuming Tafel approximations, the current density for each of the reaction is given by the anodic current density

$$i_1 = i_{0,1}\left(\theta_{H_2PO_2}\right)\left(\theta_H\right)^2 \exp\left(\frac{\alpha_1 n_1 F}{RT}\eta_1\right) \tag{18}$$

Cathodic current densities are defined as:

$$|i_2| = i_{0,2}\left(\theta_{H_2PO_2}\right)^2\left(\theta_H\right)\exp\left(-\frac{\beta_2 n_2 F}{RT}\eta_2\right) \tag{19}$$

$$|i_3| = i_{0,3}\left(\theta_{Ni}\right)\exp\left(-\frac{\beta_3 n_3 F}{RT}\eta_3\right) \tag{20}$$

$$|i_4| = i_{0,4}\left(\theta_{Zn}\right)\exp\left(-\frac{\beta_4 n_4 F}{RT}\eta_4\right) \tag{21}$$

$$|i_5| = i_{0,5}\left(\theta_H\right)^2 \exp\left(-\frac{\beta_5 n_5 F}{RT}\eta_5\right) \tag{22}$$

where η_j is the overpotential for the respective reactions. The overpotential for each reaction is given by the relation

$$\eta_j = E_m - E_{eq,j} \tag{23}$$

where E_m is the mixed potential of the deposition process and $E_{eq,j}$ is the equilibrium potential for the respective reaction as determined by the concentration of the species involved in the reaction. The equilibrium potential for each reaction is given by

$$E_{eq,j} = E_{0,j} + \frac{2.303RT}{n_j F} \log \frac{\prod c_{oxi}}{\prod c_{red}} \qquad (24)$$

where E_o is the standard potential for each reaction. For simplicity, the activity of $H_2PO_3^-$ and HPO_3^{2-} is assumed to be unity for determining the equilibrium potentials of reactions 1 and 2. However, for the case of Zn and Ni, the equilibrium potentials was found using the following relation as they are present in the complexed form

$$E_{eq,j} = E_{0,j} + \frac{2.303RT}{n_j F} \log K_j + \frac{2.303RT}{n_j F} \log \frac{\prod c_{oxi}}{\prod c_{red}} \qquad (25)$$

where K_j is the stability constant of the complexed species.

Determination of Concentration of Complexed Zn and Ni Species.

It can be seen from equation 25 that in order to determine the equilibrium potential for Ni and Zn reduction reactions, it is necessary to estimate the concentration of Zn and Ni complexed species. This was done by calculating the equilibrium concentrations of Ni and Zn species as a function of bath pH. According to Pourbaix [41], both Zn^{2+} and Ni^{2+} ions will precipitate as $Zn(OH)_2$ and $Ni(OH)_2$ respectively at pH values greater than 7.0. For the deposition to be carried out in alkaline conditions, it is necessary use of complexing agents to prevent the metal ions from spontaneous precipitation. In the presence of ammonia, the following complex ions are formed:

$$Zn(OH)_2 + 4NH_3 \rightarrow Zn(NH_3)_4^{2+} + 2OH^- \qquad (26)$$

$$Ni(OH)_2 + 6NH_3 \rightarrow Ni(NH_3)_6^{2+} + 2OH^- \qquad (27)$$

The equilibrium concentrations of the complexed species of Ni and Zn were found out by solving material balances along with equilibrium relations and electroneutrality condition. The results are shown in Figure 1. The concentration of the Ni and Zn complexed ions is seen to decrease with increase in pH. The governing equations and the computational details are summarized in the appendix.

The above equations are solved simultaneously to obtain the unknown quantities, namely, the partial current densities along with the mixed potential for the deposition process. Once the

partial current densities are obtained, the weight of each element (Ni, Zn & P) deposited are obtained using the Faraday's law:

$$m_j = \frac{M_j i_j t}{n_j F} \tag{28}$$

The weight percentages of the elements were then obtained from the calculated weights of the elements. The data obtained from the model were compared with the experimental results to check the validity of the assumed mechanism for the deposition process.

The parameters used in the model for fitting the experimental results are shown in Table 2. The kinetic parameters for the different reactions are also shown in Table 2. A part of the kinetic parameters which were not available in literature were assumed in this study.

Effect of the Substrate on the Electroless Deposition

Our initial studies indicated that zinc cannot be deposited auto-catalytically in the absence of nickel ions from the electrolyte given above. The measured mixed potential in the same electrolyte was found to depend upon the concentration of zinc ions in the bath and varied between -1.071 V *vs.* SCE (5 g/L) $ZnSO_4$ and -1.036 V vs SCE (20 g/L $ZnSO_4$). On the other site, it was possible to deposit Zn-Ni alloy at -1.036 V vs. SCE electrochemically or by using electroless technique when nickel ions were present in the electrolyte, indicating that the nickel catalyzes the zinc deposition at this potential. To determine why zinc deposits in the presence of nickel ions, the hypophosphate oxidation was carried out on nickel substrate in the presence of only complexing agents. The cathodic and anodic reactions of any of the autocatalytic processes are independent when they occur simultaneously. Thus, it is possible to study the anodic polarization of hypophosphate in the presence and absence of ions on different catalytic surfaces because it would represent the true anodic current that would occur in the complete bath. The hypophosphate oxidation curve obtained on nickel is shown in Figure 2. As shown in this figure, the nickel surface catalyzes the hypophosphate oxidation reaction since an anodic current attributable to the oxidation of hypophosphate was not observed on copper or iron. Thus, in case of electroless deposition of Zn-Ni alloys, the reaction is initiated by a spontaneous displacement reaction between iron substrate and the nickel ions present at the interface. As a result, iron dissolves while nickel deposits on the surface. The formed thin nickel film causes the oxidation

of hypophosphate to occur at potentials higher than -1.0 V *vs.* SCE, which enables zinc reduction and formation of Ni-Zn-P alloy.

Figure 3 shows the dimensionless concentration profile for each of the reacting species near the electrode surface as predicted from the mathematical model. The concentration of the hydrogen ions at the electrode surface drops to zero, suggesting that the diffusion process controls the hydrogen evolution reaction. This can be expected due to the low concentration of the H^+ ions in the electrolyte at pH 10.5. The other reactions are controlled by the electrochemical reactions at the electrode surface.

Figure 4 shows the Evans diagram for the deposition process for a $ZnSO_4$ concentration of 5 g/L. The graph shows the anodic reaction, which is the oxidation of hypophosphite given by reaction 1. The figure also shows the various cathodic reactions which occur during the deposition process. The intercepts for the different reactions were calculated based on the effective exchange current density, given by the product of the equilibrium exchange current density and the surface coverages of the species involved in the reaction as given by the equations 18-22. It can also be seen that the partial current density for Ni deposition is high followed by those of Zn and P deposition. The potential at which the oxidation line and the overall reduction line crosses is the mixed potential of the deposition process and the current density at that point corresponds to the electroless plating current density.

Figure 5 compares the predicted and experimental mixed potential values and plating current densities as a function of $ZnSO_4$ concentration in the bath. It can be seen from the plot that the mixed potential becomes more positive as a function of $ZnSO_4$ concentration. This result is consistent with the experimental observation where the addition of Zn ions shifts the deposition potential to more positive values. The experimental current densities were obtained by calculating the current required for the deposition of different elements using Faraday's law. It can be seen that the plating current densities predicted by the model is marginally higher than the experimental values. This can be expected, as the experimental values do not include the current due to hydrogen evolution reaction. It can also be seen that the plating current density decreases as a function of $ZnSO_4$ concentration. This result suggests that the addition of Zn ions inhibits the deposition process. This inhibition effect of Zn on the deposition process has been reported

previously [25] and was also observed in our study [28]. In order to further analyze the effect of Zn ions on the deposition process, linear polarization studies were used.

Ohno *et. al.* used linear polarization and impedance techniques to predict the plating rate of an electroless process. According to Ohno *et. al.*, the plating current density is equivalent to the reciprocal value of the polarization resistance [33]. The relationship between the plating current density and the polarization resistance is given by the equation:

$$\frac{i_{pl}}{K} = \frac{1}{R_p} \tag{29}$$

Where K is a constant related to the deposition process being studied. This method is similar to the Stern-Geary relation for predicting the corrosion of a metal, although the implication in the case of electroless deposition is different. Ohno *et. al.* used this method successfully to predict the plating rate of an electroless copper deposition process [33]. In order to study the inhibitive nature of Zn ions on the Ni-Zn-P deposition process, linear polarization studies were performed to obtain the polarization resistances as a function of the Zn ions in the bath. Linear polarization studies were obtained by scanning the potential 10 mV above and below the mixed potential after initiating the deposition process. The results are shown in Figure 6. As shown in this figure, the addition of Zn ions in the bath increases the polarization resistance suggesting that Zn ions inhibit the deposition process.

This inhibitive effect of Zn ions on the deposition process was also confirmed by an alternate method. With a decrease in the plating rate, it can be expected that the moles of hypophosphite ions consumed during the reaction also to decrease. Hence, the consumption of hypophosphite ions was determined by the iodometric titration analysis as a function of $ZnSO_4$ concentration in the bath. The consumption of hypophosphite was determined by calculating the moles of hypophosphite in the bath before and after the deposition process. With an increase in Zn ion concentration in the bath, the moles of hypophosphite consumed during the reaction decrease, thereby indicating a decrease in the deposition rate.

Figure 7 shows the surface coverage of all electro active species participating in the deposition process as a function of $ZnSO_4$ concentration in the bath as predicted by the model. With an increase in Zn ion concentration in the bath, the surface coverage of Ni ions decreases and that of the Zn ions increases. This result is in agreement with the assumption made in the

model that Zn ion inhibits the Ni adsorption on the surface. This variation in the adsorption of the reacting species results in the reduction of the plating current. However, in Figure 7, the surface coverage of hypophosphite ions increases with increase of zinc ion concentration in the bath which does not agree with the overall plating current density, i_{pl} decrease observed in Figure 5. In other words, one can expect an increase in the overall current density with an increase in hypophosphite ion surface coverage. The results can be explained by taking into account that the effective exchange current density for hypophosphite oxidation is also controlled by the square of the hydrogen ion surface coverage, Eq. (18). The increase in hypophosphite ion concentration results in a decrease of hydrogen ion surface coverage, thereby reducing the effective exchange current density for hypophosphite oxidation. The effective exchange current density for hypophosphite decreases from 4.9 x 10^{-7} A/cm^2 to 6.7 X 10^{-8} A/cm^2 when the Zn ion concentration is increased from 5 g/L to 20 g/L. This results in reducing the current for hypophosphite oxidation, thus reducing the overall plating current density. These results show clearly that the concentration of Zn ions in the bath plays an important role in determining the rate of the deposition process.

Figure 8 shows a comparison between the weight percentages of Ni obtained from the model and experiments as a function of $ZnSO_4$ concentration in the bath. The plot shows good agreement between the experimental results with those of the model. The Ni content in the deposit decreases as a function of Zn concentration in the bath. This result can be expected since the Zn ions inhibit the adsorption of Ni ions on the surface, thereby reducing the Ni content in the deposit.

Figure 9 shows the variation in the Zn and P content in the deposit as a function of $ZnSO_4$ concentration in the bath. The Zn content in the deposit increases as a function of Zn ion concentration. This result can be expected as the partial currents for each reaction is proportional to the surface coverages of the adsorbed species. It was shown in Figure 7 that the surface coverage of Zn ions increases with an increase in $ZnSO_4$ concentration in the bath. This change in surface coverages results in the deposition of a significant amount of Zn (10-17 wt%) in the deposit.

Another important parameter that affects the deposition process is the pH of the bath. Figure 10a shows the effect of pH on the mixed potential for the deposition process. The figure

shows that an increase in pH makes the mixed potential more negative. With increase in pH of the bath, the potential for the hypophosphite oxidation shifts to more negative values. This shift in potential is expected to move the mixed potential to more negative values leading to an increase the plating current density, since the overpotential for each reaction increases. Thus, by increasing the pH of the electrolyte one can increase the deposition rate. Figure 10a also shows the effect of pH on the plating current density. Increasing the pH of the bath results in increasing the plating rate of the deposition process.

Figure 10b shows the surface coverage of the reacting species as a function of the bath pH. Figure 11 shows the variation in the Ni, Zn and P content in the deposit as a function of pH of the bath. The figure also shows the comparison of the composition of the coating obtained from the model with the experimental results.

Part 2. Optimization Studies for the Electrolytic Ni-Zn Process:-

Effect of Zn^{2+} ions on the coating composition:

The primary objective of this work was to obtain a nickel rich sacrificial coating for the protection of steel. Thus, it is essential to estimate the amount of Zn in the final deposit. EDAX analysis was used for this purpose. Depositions were carried with different concentrations of $ZnSO_4.7H_2O$ in the bath with an applied potential of -1.3 V (vs. SCE). Figure 12 shows the distribution of Zn and Ni in the coating as a function of $ZnSO_4$ added in the bath. It can be seen from the plot that the Zn content in the deposit increases from 26-wt% in the case of 5 g/L $ZnSO_4$ to 53-wt% in the case of 30 g/L $ZnSO_4$. The amount of Ni decreases from 74-wt% to 47-wt% with increase of $ZnSO_4$ concentration in the bath. Increase of Zn content in the deposit is mainly due to the increase in the concentration of Zn ions available for competing with the deposition of nickel. In order to obtain nickel rich alloys with uniform morphology, further depositions were carried out with 15 g/L $ZnSO4.7H_2O$ in the bath.

Cathodic Polarization:

Cathodic polarization curves were plotted to analyze the inhibiting nature of the zinc ions present in the solution. Fig 13a shows the cathodic polarization curve recorded from a solution of 71.1 g/L of sodium sulfate, 50 g/L of ammonium sulfate and 30g/L of sodium citrate at pH 10.5 in the presence and absence of 15 g/L of $ZnSO_4.7H_2O$ in the solution. It can be observed that in

the absence of any zinc ions in the solution, the current recorded corresponds to that of the hydrogen reduction accompanied with water hydrolysis. When zinc ions are added to the solution, the hydrogen evolution reaction is strongly suppressed. This phenomenon occurs even at potentials below the reduction potential of zinc. This observation emphasizes that zinc ions strongly adsorb on the surface of the substrate.

Fig 13b shows the cathodic polarization curve recorded from the alkaline bath when only nickel ions is present and when both nickel and zinc ions are present. When zinc ions are added in to the solution, the current density at the nickel deposition drastically decreases. In other words, nickel ions need to compete with the zinc adsorbed species for deposition leading to its inhibition in the presence of zinc ions. Inhibiting behavior of Zn is further confirmed with the plot of partial current density of Zn and Ni during alloy deposition and single metal deposition as shown in Fig 14. During single metal deposition, the concentration of electroactive species is maintained constant by substituting the respective alloying metal with magnesium sulfate of equal concentrations. It can be observed that the partial current density of nickel drastically decreases in the presence of zinc ions. Single metal deposition of Zn under similar conditions is observed only at potentials above -1.3 V vs. SCE. However, the zinc partial currents showed that in the presence of nickel, zinc can be deposited at potentials where it does not deposit in the absence of nickel ions. The deposition of zinc could be due to the presence of some form of adsorbed species such as $ZnNi^{+}_{ads}$ [38, 42, 43].

Effect of Applied Potential:

Figure 15 shows the variation in the composition and deposition rate of the coating as a function of the applied potential. The thickness of the coatings was estimated by dividing the weight of a unit area with the average density of the alloy. For an applied potential of –1.0 V *vs.* SCE, the thickness of the deposit is very low (0.5 μm). An increase in the applied potential resulted into an increase in the thickness of the deposit. EDAX analysis results in detecting elemental distribution to a depth of 1 μm. If the coating thickness is less than 1 μm, the underlying substrate constituents are also detected. At an applied potential of –1.0 V *vs.* SCE, the coating thickness is less than 1 μm and hence Fe is detected. However, with an increase in applied potential, the Fe content decreases and reaches a value of <0.1-wt% at potentials greater than –1.1 V vs. SCE. This trend shows that operating at a potential below –1.1 V gives rise to

uniform coatings with thickness greater than 1 μm. Increasing the deposition potential leads to an increase amount of Zn in the deposit, suggesting that the deposition becomes more anomalous in nature. Similar results were obtained by Roventi *et. al.* [38]. However, they have also observed that the deposits obtained at low potentials have high stress and had powdery appearance with poor adhesion. Hence, such deposits cannot be used as a sacrificial coating. However, for the present case of Ni-Zn alloys deposited from alkaline bath at low potentials, no cracks were observed on the coating. The deposition from alkaline baths provided a wide window of potential from which nickel rich alloys can be deposited.

Figure 16 shows the SEM micrographs of Ni-Zn alloy deposited at different potentials: -1.0 V, -1.1 V, -1.3 V and -1.5 V (vs. SCE). SEM photographs show that deposits obtained at -1.0 V are smooth and with average particle size of the deposit in the order of 20 nm ~ 60 nm. It can be observed that the deposit plated at -1.1 V (vs. SCE) was smooth with a particle size of 1 micron. When the potential was increased to -1.3 V (vs. SCE) and above, the zinc content in the deposit increases as observed from the well defined crystals, which are characteristic for zinc deposits. The nickel content can be varied in the alloy from 78 % to 40 % by varying the applied potentials. The amount of nickel in the deposit for the corrosion protection was optimized by studying the corrosion properties of all deposits synthesized in this study.

To estimate the suitability of the coating as a sacrificial coating, the corrosion characteristics of the deposits were tested in a 0.5 M Na_2SO_4 + 0.5 M H_3BO_3 solution at pH 7.0. Tafel polarization was performed to evaluate the corrosion rates of the coatings with different Zn contents. Tafel studies were carried out by scanning the potential from –200 mV to +200 mV with respect to the corrosion potential at a scan rate of 10 mV/s. The resultant Tafel plots are shown in Figure 17. As shown in the plot, the corrosion current of the deposits increases with increase in the amount of Zn content in the deposit. This is due to the fact that with higher amounts of Zn in the deposit, the dissolution rate of the alloy is increased. The corrosion potential also shifts to a more negative value with increase in the Zn content. Table 3 summarizes the corrosion potential and the corrosion rate of the coating as a function of Zn content in the deposit. Tafel polarization studies indicated that the alloy containing 28% of Zn has optimum corrosion resistance.

Effect of pH:

The pH of the electrolyte plays a very important role in determining the composition of the Ni-Zn deposit obtained. A complete analysis of the equilibrium reactions between various species is performed to analyze the effect of pH. According to the pH –potential diagrams of zinc and nickel by Pourbaix, the zinc and nickel precipitate to form their respective hydroxides with increase in pH beyond 7.00. The presence of complexing agent like ammonia prevents the precipitation. In the presence of ammonia, the following complexes are expected to be formed.

$$Zn(OH)_2 + 4NH_3 \rightarrow Zn(NH_3)_4^{2+} + 2OH^-$$

$$Zn^{2+} + 2OH^- \rightarrow Zn(OH)_2$$

$$Ni^{2+} + 2OH^- \rightarrow Ni(OH)_2$$

$$Ni(OH)_2 + 6NH_3 \rightarrow Ni(NH_3)_6^{2+} + 2OH^-$$

Zn and nickel complexes reduce to deposit as Zn-Ni alloy with the liberation of ammonia.

$$Zn(NH_3)_4^{2+} + 2e^- \rightarrow Zn + 4NH_3$$

$$Ni(NH_3)_6^{2+} + 2e^- \rightarrow Ni + 6NH_3$$

Ni-Zn deposition was performed at different pH ranging from 8.5 to 9.5. Figure 18 shows the variation in composition of the zinc and nickel in the deposit as a function of pH. With increase in pH, the nickel content in the deposit starts to increase and above pH of 10.5 it stabilizes. The results agree well with the pH concentration diagram. With increase in pH a higher concentration of nickel was observed in the deposits. Thus, the pH of the electrolyte was optimized to be 10.5.

Effect of Temperature:

Another critical parameter that affects the composition of the coating is the temperature of the bath. Fig 19 shows the variation in the composition of the deposit as a function of bath temperature. The nickel content in the deposit increases linearly with increase in temperature. An increase in nickel content from 34 % to 61 % was observed by increasing the temperature to 60°C. Fig 20 presents the variation in thickness with temperature. At temperatures above 60 °C, no significant variation of the composition is observed. At these temperatures the deposition rate increases. However, an increase of temperature 60°C leads to increase in the internal stress and develops cracks in the deposits. Thus, the deposition temperature was optimized to be 60 °C.

Part 3: Development of Novel Zn-Ni-Cu ternary alloy:

Figure 21 represents the EDAX analysis for a conventional Zn-Ni alloy that exhibits anomalous behavior and that of a Zn-Ni-Cu alloy. The Zn:Ni ratio in the commercial alloy was as high as 7.5 : 1. With the addition of 1g/L of $CuSO_4$ in the bath, the ratio of Zn:Ni decreases to 1.3 : 1. It was observed that the Zn:Ni ratio can be varied with the use of the ternary alloying element copper. Now we proceed step by step to obtain an insight into the deposition process of Zn-Ni-Cu.

Stripping Cyclic Voltammetry:

Stripping cyclic voltammograms (SCV) were obtained to analyze the behavior of the Zn-Ni-Cu deposition process. Electrodeposition of the Zn-Ni-Cu was performed on a gold rotating disc electrode of 0.458 cm^2 area. The composition of electrolyte used was 40 g/L of $NiSO_4.6H_2O$, 20 g/L of $ZnSO_4.7H_2O$, 71 g/L of Na_2SO_4 and 1 g/L of $CuSO_4$. The potential was varied at a scan rate of 30 mV/s from –0.5 V (vs. SCE) to a cathodic potential of –1.4 V (vs. SCE) and back to the initial potential, –0.5 V (vs. SCE). This potential range is representative of the hydrogen evolution and metal dissolution reactions occurring at the surface of the coating under normal corroding conditions. Figure 22 represents the SCV analysis of Zn-Ni-Cu deposits obtained at different rotation speeds. Deposition of Zn, Ni and Cu takes place during the forward cathodic scan. Beyond a potential of –1.1 V (vs. SCE), the steep increase in the current can be attributed to the hydrogen evolution reaction. During the reverse scan distinct current peaks were observed. These peak currents are attributed to the dissolution of the metal alloy components. The first dissolution peak occurring at –0.77 V (vs. SCE) corresponds to the zinc dissolution [21]. The second anodic peak occurring at –0.43 V (vs. SCE) can be attributed to the dissolution of the nickel rich phase. The final dissolution peak in the anodic scan corresponds to the dissolution of the copper rich phase. The SCV's were performed at three different rotation speeds to determine the mass transfer effect limitations on the deposition process. The peak currents corresponding to the Zn and Cu dissolution potentials increase with increase in the rotation speed, indicating the mass transfer controlled nature of the deposition processes. These are in agreement with the previous studies [21]. On the other hand, nickel deposition is kinetically controlled [25]. The dissolution peak decreases with increase in rotation speed. The observed decrease in the nickel

peak current is due to the effect of side reactions that are under mass transfer control. With this preliminary knowledge of the deposition process, we next proceed to study the effect of electroactive species on the composition of the deposit.

Effect of $CuSO_4$ concentration:

To analyze the effect of CuSO4 concentration on the ratio of Zn and Ni, depositions were carried out from an alkaline bath of 60 g/L $NiSO_4.6H_2O$, 30 g/L $ZnSO_4.7H_2O$, with the amount of copper sulfate varied between 0.5 g/L and 4 g/L. The bath pH was maintained at 9.0 and depositions were carried out potentiostatically at different potentials without stirring. Figure 23 represents the effect of $CuSO_4$ concentration and deposition potential on the composition of the deposit. It is observed that at low potentials, copper and nickel deposition dominate the process resulting in increased content of copper and nickel in the deposit. The Zn content is as low as 30% in the presence of 0.5 g/L of $CuSO_4$. This is due to the low applied potential of the deposit. With increase in the deposition potential, Zn content in the deposit increases with decrease in the nickel and copper composition. The addition of $CuSO_4$ in the sit, alters the Zn-Ni ratio. When deposited at -1.3 V (vs. SCE), the nickel content increases from 12.4% (not shown in Fig 3) to 25 % with the addition of 0.5 g/L of $CuSO_4$ in the Zn-Ni bath. When the concentration of CuSO4 is about 1g/L, the nickel content is as high as 31 %. It can be observed that the nickel content in the deposit increases with the addition of $CuSO_4$ in the bath. The increase in the concentration of $CuSO_4$ in the bath leads to an increase in the copper content in the deposit. Anomalous deposition of Zn-Ni is due to the preferential adsorption of Zn ion on the depositing surface. The adsorption is not necessarily, electrochemical in nature. Presence of Cu ions in the solution decreases the preferential adsorption of zinc ions to the surface there by favoring the nickel deposition. But with the concentration of $CuSO_4$ in the bath 2 g/L and beyond, copper deposition dominates the whole process leading to a decrease in both Ni and Zn content. The decrease in Ni content is less pronounced compared to that of Zn. To have a better insight in to the deposition process, the partial current densities were calculated using faraday's law. Figure 24 shows the plot of partial current density as a function of applied potential and concentration of $CuSO_4$. When the concentration of $CuSO_4$ in the bath is less than or equal to 1 g/L, the limiting current of Cu is lower than the partial current density of Ni. As seen from our preliminary studies with SCV, Zn and Cu are mass transfer controlled. Since Cu is mass transfer controlled, the

concentration of the Cu in the deposit does not increase once the limiting current density for the deposition is reached. However, further increase in the concentration of the $CuSO_4$ in the bath lead to an increase in the limiting current density of copper. When the limiting current density of Cu exceeds the partial current densities of Ni and Zn, Cu deposition dominates the whole process. As high as 80 % of Cu was observed in the deposit when the concentration of $CuSO_4$ was 4g/L and further increase in the potential showed minimal change in the composition of the deposit. Hence the prominent factor in determining the composition of the deposit is the concentration of $CuSO_4$ in the bath.

Effect of Stirring:

As seen from our preliminary studies, Zn and Cu deposition are mass transfer controlled and Nickel deposition is kinetically controlled. Hence stirring has a significant effect on the deposition kinetics. Studies were performed under different stirring conditions. Depositions were carried at –1.3 V (vs. SCE) from a solution containing 30 g/L of $ZnSO_4.7H_2O$, 60 g/L of $NiSO_4.6H_2O$ and 1g/L of $CuSO_4$, at a pH of 9.0. From Figure 25, it is observed that increasing the stirring speed increases the percentage of Cu in the deposit while it decreases the Ni content. The observed increase in the Cu content can be explained by the kinetics of the deposition processes. The Cu and Zn deposition are mass transfer controlled processes and stirring increases the concentration of the Cu and Zn electroactive species available at the interface for the deposition. But owing to its low deposition potential, copper deposition dominates. Also, the increased concentration of the Cu and Zn species increases the deposition rate. The observed decrease in the Ni content results from mass transfer control of the competing proton, Zn and Cu reduction processes.

Effect of $ZnSO_4.7H_2O$ concentration:

The concentrations of the electroactive species in the bath play a significant role in determining the composition of the alloy. This is due to the kinetics of the deposition processes. Figure 26 shows the variation in composition of the alloy as a function of the $ZnSO_4.7H_2O$ concentration in the bath. Depositions were made from 60 g/L of $NiSO_4.6H_2O$ and 1 g/L of $CuSO_4$, pH 9.0 at –1.3 V (vs. SCE). It is observed that the zinc content in the deposit increases with increasing $ZnSO_4.7H_2O$ in the bath. The Cu and the Ni contents decrease. In the case of 1 g/L of $CuSO_4$ in the bath, the increase in zinc content in the deposit is well pronounced with

increase in $ZnSO_4.7H_2O$ concentration in the bath. But when the concentration of $CuSO_4$ in the deposit is 4 g/L, an increase in the concentration of $ZnSO_4.7H_2O$ in the solution doesn't have significant change in the composition of the deposit. Copper was found to dominate the alloy composition. Thus it becomes imperative to fix the concentration of $CuSO_4$ less than 1g/L. Also, increase in the Zn content shifts the corrosion potential to more negative value, leading to a decrease in the corrosion resistance of the coating. From the studies, the concentration of $ZnSO_4.7H_2O$ should be 30 g/L for an optimum Zn:Ni ratio in the deposit.

Figure 27 shows the effect of $ZnSO_4.7H_2O$ on the current density as function of deposition time. It can be observed from the figure that when the concentration of $ZnSO_4.7H_2O$ is 10g/L, the current density follows a unique pattern. The current density is stable up to 2000 seconds and increases steeply after that. On increasing the concentration of $ZnSO_4.7H_2O$ the stable plateau of the current density increases. Such changes in the current density modify the morphology and composition of the deposits. EDX analysis and SEM micrographs were used to characterize this pattern. Figure 28 shows the surface morphology of coatings taken at three points indicated in the previous figure. It can be observed that the morphology of the coating in the stable plateau region was uniform and good. The composition of the deposit was 47/32/21 for Zn/Ni/Cu and was uniform through out the deposit. At the point 2, where current density starts to increase, it can be observed dendritic growth is initiated. The dendrites were rich in copper and nickel. EDX point analysis at the dendrite showed a composition of 18/42/40. SEM morphology at the steady state region, point 3 shows the deposit filled with dendrites. EDX analysis shows the composition of the deposit to be as 28/37/35 for Zn/Ni/Cu respectively. With the growth of dendrites, nickel and copper deposition is favored. But such a composition will bring down the corrosion potential of the coating less than that of Fe which is not desirable in our case. Moreover, the due to dendritic growth, the adherence of the deposits is poor. The deposits are powdery and get removed from the surface with washing. This imposes a limit on the thickness of the adherent film. Increasing the concentration of $ZnSO_4.7H_2O$ increases the stable plateau of current density and thick films can be grown. But increase in $ZnSO_4.7H_2O$ increases changes the composition of the deposit and there by the corrosion properties. Hence additives were tested to improve the adherence of the deposits to the substrate. Addition of 0.5 g/L of dextrin and 60g/L of sodium citrate to the deposition bath yielded a constant current density and a uniform deposit.

Figure 29 shows the SEM morphology of the deposit obtained in the presence of additives. The deposit was homogenous and dense with well organized structure compared those prepared in the absence of additives. EDX analysis shows uniform concentration of 45/35/20 for Zn/Ni/Cu respectively. Also the current efficiency of the process increases.

Part 4: Corrosion Characteristics of the Coatings:

As the whole endeavor of our work is to develop sacrificial coatings that can replace cadmium, it is critical to compare the performance of the developed coatings to Cadmium and other sacrificial coatings. The coatings that have been chosen for comparison in this study are Zinc, Zinc-Nickel and Cadmium, as these are the most commonly used sacrificial coatings for protection of steel. The thicknesses of the various coatings were approximately 2 μm for these comparison studies. The deposit thickness was estimated by dividing the weight of a unit area with the average density of the alloy. All the corrosion studies were performed in a ph 7.0 solution of 0.5 M Na_2SO_4 and 0.5 M H_3BO_3 unless and other wise specified.

Linear Polarization:

Linear polarization studies were carried out to find the polarization resistances of the various coatings. The potential was swept from -10 mV to +10 mV vs. E_{corr} at a scan rate of 0.5 mV/s. The resulting graphs of overpotential *vs.* current density for the different coatings are shown in Figure 30. The slope of these lines yields the value of the polarization resistance. The low polarization resistance for the Zn and Zn-Ni alloy coatings show that the corrosion rates for these coatings are much higher than the Zn-Ni-Cu, Ni-Zn and Ni-Zn P (Electroless) coatings developed in our laboratory. Table 4 shows the various coatings that have been chosen for comparison along with the E_{corr} values and corrosion currents. The corrosion rates have been calculated using the polarization resistance found from the linear polarization technique. Figure 30a summarizes the corrosion rates obtained for various coatings in the form of a bar plot. The bar plot shows the superior corrosion characteristics of the coatings developed in our laboratory as compared to the other sacrificial coatings.

Electrochemical Impedence Spectroscopy:

EIS was used to evaluate the barrier properties of the coatings and to determine the polarization resistance and the corrosion rates with out modifying the surface. Figure 31 represents a comparison of Nyquist responses obtained for Zn, Zn-Ni, Cd, Zn-Ni-Cu, electrolytic

Ni-Zn and electroless Ni-Zn-P coatings. The solution resistance remains the same for all the deposits. This is to be expected since the studies were done under similar conditions in pH 7.0. R_p values can be approximately determined by fitting the Nyquist response to a simple equivalent circuit consisting of ohmic resistance, double layer capacitance, and polarization resistance. Nickel coating possesses a high polarization resistance of 5800 ohms (not shown in Figure 31). This is obvious owing to the high barrier properties of nickel coating. The electrodeposited Ni-Zn alloy and electroless Ni-Zn-P offers a barrier resistance in the order of 2000 ohms, which is five times higher than the typical Cd deposit. The increase in the barrier resistance of these coatings is an outcome of the increase in nickel content in the deposit.

Stability of the Coatings:

The sacrificial properties as predicted by the OCP measurements were verified using the scratch-model approach. The more negative zinc coatings offer high level of sacrificial protection to the underlying steel and inhibit the hydrogen penetration in the bulk of the alloy. However this coating has very short life due to a high rate of galvanic corrosion. The potential of pure zinc was stable at –1.1 V (*vs.* SCE) whereas, the OCP's of Zn-Ni and Zn-Ni-Cu, Ni-Zn and Electroless Ni-Zn-P were more positive indicating that inclusion of more noble components in the deposit results in the anodic shift in potentials with respect to zinc which in turn decreases the galvanic corrosion. The potentials of Zn, Zn-Ni, Cd, Zn-Ni-Cu, Ni-Zn and Ni-Zn-P deposits were continuously monitored with respect to SCE as a function of time. The results presented as potential-time plateaus are shown in Figure 32. The OCP plots of Zn-Ni showed three distinct plateaus occurring at three different potential namely -1000 mV, -700 mV and –400 mV.

Zn-Ni alloys deposit in three phases, a Zn-rich phase called eta (η) phase (E_{corr} = -1.050 V *vs.* SCE), an intermediate gamma phase, (γ), (E_{corr} = -0.700 V *vs.* SCE) and a nickel rich alpha (α) , E_{corr} = -0.400 V *vs.* SCE) phase. The η phase has a rest potential comparable to that of pure zinc since it is mostly composed of zinc. The Zn-rich η phase deposits exhibit homogenous hexagonal shaped crystals, but once a galvanic couple is formed, they dissolve rapidly and the surface becomes enriched in the γ phase. The intermediate phase or the γ phase, which has a Zn-Ni ratio of 4:1, is body-centered cubic structure and usually represents a good barrier resistance against dissolution. However, the thickness of this layer is so small that it vanishes for short

period of time. Dissolution of γ phase exposes the nickel rich phase to the environment. A small defect in the coating in such a case would lead to the preferential dissolution of the less noble metal namely steel. Thus, an increase in life of the protective coating depends on the life of the more electronegative phase, which is Zn rich η phase in case of Zn-Ni coatings. The commercially available coating like Zn, Zn-Ni and cadmium lasted for less than 60 hrs. the Ni-Zn and Electroless Ni-Zn-P alloys prolonged for more than 100 hrs. The potential remained constant for these alloys. In the case of Zn-Ni-Cu, the potential remained constant till 100 hours before it started to decrease. Ni-Zn and electroless Ni-Zn-P alloys prolonged for more than 100 hrs. The potential remained constant for these alloys. These studies emphasize the superior corrosion and sacrificial properties of the electrolytic Ni-Zn and electroless Ni-Zn-P.

Mechanical Properties:

Table 5 tabulates the mechanical properties of the various coatings being tested along with their composition obtained using EDAX analysis. As seen from the table, all the coatings were seen to possess good adhesion to the underlying substrate. There was no visible flaking or detachment of the coatings from the substrate when the sample was returned to its original profile, after subjecting it to a bending of 180°. Abrasion index was used as a measure for comparing the abrasion resistance of the coatings and is given by the amount of material lost in mg after being subjected to 200 cycles of abrasion. Care was taken that no interference is seen from the substrate during the test. From the experiments, it was seen that the electrodeposited Zn-Ni alloys have poor abrasion resistance losing 18.5 mg after 200 cycles of abrasion. However, Ni-Zn-P alloys were seen to provide much higher abrasion resistance, losing only 8 mg of material that is close to that of Cd coating (6 mg). Finally, the hardness of the coating was determined in a microhardness measurement unit by applying a force of 25 gpf for 10 seconds and then measuring the length of the indents with the help of a microscope. The microhardness, reported as Knoop's Hardness Number (HK_{25}), of the coating were measured using the formula,

$$Microhardness = \frac{1.854 \times 10^6 \times F}{L^2} \qquad (30)$$

where, F is the applied force in kgpf and L is the length of the indent in μm.

From the table, it can be seen that the hardness of Ni-Zn-P alloys is comparable to that of Cd coatings, whereas the hardness of electrodeposited Zn-Ni alloys with 5.4-wt% Ni is much lower.

The reason for this higher hardness of Ni-Zn-P than Zn-Ni alloy could be due to the increased amount of Ni in the alloy. To confirm this, Zn was electrodeposited from an acidic bath and when subjected to the hardness testing, it gave a hardness number of 82 HK_{25}, which is comparable to the value reported for Zn deposits in literature. From these results, it can be seen that the Ni-Zn-P alloys possess engineering attributes similar to those of Cd coatings.

CTC Results:

Electrolytic Ni-Zn and Ni-Zn–P was tested in the Naval Aviation Center (NAVAIR) for the replacement of cadmium coatings. One of the primary requirements for the substitution of cadmium is that no signs of white rust or red rust should be found after 96hrs in an unscribed and scribed salt fog testing as per ASTM B117-94 specifications. The scribed salt for showed no rust in the scribed area for the Ni-Zn and electroless Ni-Zn-P coatings. This confirms the superior corrosion and sacrificial properties of the electrolytic Ni-Zn and electroless Ni-Zn-P. These coatings suffered from adhesion problems under CTC testing. The process used then was in its preliminary stages. In the past on year these processes have been improved considerably. Currently corrosion tests based in ASTM B117 specification is in progress with our newly acquired salt fog chamber. The results are expected soon.

Part 5: Hydrogen Permeation Studies on Ni-Zn-P alloys:

Hydrogen Permeation Characterization:

Figure 33 shows the variation in the hydrogen permeation current of the Ni-Zn-P deposited steel membrane as a function of time. Applying different cathodic overpotentials varied the permeation currents through the membrane. Prior to any application of overpotential to the cathodic side of the bipolar electrode, the background current on the anodic side was allowed to stabilize below 0.5 $\mu A/cm^2$. Subsequently, the cathodic side of the membrane was polarized in the negative direction so as to provide conditions for hydrogen evolution. Hydrogen that comes out of the anodic side after a series of adsorption-absorption-diffusion steps is oxidized potentiostatically to obtain the permeation current. The hydrogen oxidation potential in 0.2 M NaOH (pH=13.0) is –1.693 V *vs.* Hg/HgO (-0.767 V *vs.* SHE). Hence applying a potential of –0.3 V *vs.* Hg/HgO to the anodic side of the bipolar electrode ensured the instantaneous oxidation of the permeating hydrogen. The steady state permeation current for each value of applied

cathodic potential was noted down. Using the same process, the hydrogen evolution and permeation currents of the Zn-Ni coated membrane were measured for each value of the applied overpotential. For the case of Cd deposited membrane, we used the data that has been previously published [60].

Figures 34 and 35 show the dependence of the hydrogen charging current (i_c) and the permeation current (i_a) for Ni-Zn-P and Zn-Ni coatings. In both the figures, the reported overpotentials have been calculated based on the open circuit potential of the coating being tested, the values of which have been reported as the corrosion potential in Table 4. For example, an overpotential of –0.3 V corresponds to an applied potential of –0.952 V *vs.* SCE for Ni-Zn-P and –1.113 V *vs.* SCE for Zn-Ni coatings. As seen from Figure 34, Ni-Zn-P coatings have two orders of magnitude lower current densities for hydrogen evolution as compared to Zn-Ni coatings. The current density for hydrogen evolution in case of Ni-Zn-P was around 8.5 x 10^{-5} A/cm^2 for overpotential of -300 mV. For a similar overpotential, the Zn-Ni coated steel exhibits a very high cathodic current density of 7.8 x 10^{-3} A/cm^2. The high hydrogen discharge currents exhibited by Zn-Ni coatings has been attributed previously to the presence of high amount of Zn [61]. In the case of electrodeposited Cd, the hydrogen evolution current density is around 6.6 x 10^{-5} A/cm^2 for a typical applied cathodic overpotential of 300 mV [60]. Figure 35 compares the permeation current densities for the Zn-Ni and Ni-Zn-P coated steel membranes. A very large decrease in the permeation current density is seen for Ni-Zn-P deposits. It must be noted that these permeation currents were calculated with respect to the steady-state permeation currents, which are non-zero, and equal 0.26 μA/cm^2 in the case of Ni-Zn-P coatings as seen in Figure 33. For an applied overpotential of –300 mV, the permeation current increased to a value of 0.64 x 10^{-6} A/cm^2 in case of Ni-Zn-P deposited steel, while Zn-Ni coatings gave a permeation current density of 7.1 x 10^{-6} A/cm^2. For Cd deposited steel, application of a similar overpotential showed a permeation current density of 2.2 x 10^{-6} A/cm^2 [60]. Comparison of these hydrogen permeation currents with that of uncoated steel at an applied overpotential of -300 mV, shows that Ni-Zn-P coatings reduces the hydrogen influx into the steel substrate by 94% as compared to 80% and 35% for Cd and Zn-Ni coating respectively. Figure 36 gives the hydrogen entry efficiency (defined as $\frac{i_a}{i_c} \times 100$) for the various coatings. The hydrogen efficiency for Cd deposited steel was calculated using data from previous analysis [60]. We can see from the graph that Ni-Zn-P

deposited steel exhibits lower hydrogen entry efficiency than Zn-Ni and Cd coatings. This shows that Ni-Zn-P coating allows lower amount of the evolved hydrogen atoms to permeate into the substrate. In order to analyze the observed decrease in permeation current for Ni-Zn-P coating, it is important to evaluate the various kinetics parameters governing hydrogen evolution and permeation for the various coatings.

Several models have been published in literature to explain the hydrogen entry into metals and to evaluate the kinetic and permeation parameters required to explain the process [53-57]. The Tafel slope and $d\eta/d\log(i_a)$ relationship that is obtained for any particular system determines the selection of an appropriate model that can be used to evaluate the kinetics parameters for hydrogen permeation. As the i_c-η slopes for Zn-Ni and Ni-Zn-P alloys has a range of 120~130 mV/decade and $d\eta/d\log(i_a)$ shows a value of 240~260 mV/decade, the coupled discharge – chemical recombination mechanism is valid for these alloys. Hence the hydrogen permeation analysis for these alloys was performed using the Iyer-Pickering-Zamanzadeh (I-P-Z) model [56]. The I-P-Z mechanistic model assumes that during hydrogen discharge on the surface, $\eta >> RT/F$ so that the backward reactions are negligible and the surface coverage is low enough so that a Langmuir isotherm can be used for the hydrogen coverage. With these assumptions and after suitable modifications, the following relationships were obtained to correlate the hydrogen charging (cathodic) current i_c and the permeation current i_a with the various kinetic parameters [18]:

$$\theta_s = \frac{\left[k_{ads} + \left(\frac{D}{L}\right)\right]}{k_{abs}} C_s = \frac{C_s}{k''} = \frac{bi_a}{k''} \tag{31}$$

$$i_a = \frac{k''}{b\sqrt{Fk_3}}\sqrt{i_r} \tag{32}$$

$$i_c e^{\frac{F\alpha\eta}{RT}} = -\frac{bi_0}{k''} i_a + i_0 \tag{33}$$

The transfer coefficient, α, required for the parameter estimation was derived by solving a quadratic equation involving S_c and S_a, the cathodic and anodic slopes obtained from Figures 34 and 35 [18]. Out of the two roots for α, the one that resulted in negative values of i_0 and k'' was neglected.

The square root of the recombination current density ($\sqrt{i_r}$) vs. the permeation current density (i_a) for Ni-Zn-P and Zn-Ni are given in Figure 37. As seen in the figure, the plots are linear and pass through the origin for Zn-Ni and Ni-Zn-P alloys, which is in agreement with equation 3. To ascertain the validity of the model further and for parameter estimation, Figure 38 is used to verify the linear dependence between i_a and $i_c e^{a\alpha\eta}$ as seen in equation 4. Figure 38 shows that both Zn-Ni and Ni-Zn-P exhibit linear slopes, thus validating the application of this model to analyze the experimental results. The slopes and intercepts in Figure 38 are used to calculate i_0 and k'' for Ni-Zn-P and Zn-Ni coated steel (the value of b is known and remains the same for both coatings). Knowing i_0 and k'', k_3 is then calculated from the slope obtained from Figure 37 for Zn-Ni and Ni-Zn-P coated steel.

The surface coverage of hydrogen was calculated using equation 31 and is plotted as a function of applied overpotential for the various coatings in Figure 39. The surface coverage in case of Ni-Zn-P and Zn-Ni coated steel remained low at all applied potentials. This result validates the assumption of Langmuir isotherm for hydrogen surface coverage and hence the application of the I-P-Z model for the case of Zn-Ni and Ni-Zn-P alloys [56].

Comparison of Hydrogen Permeation Properties:

Table 6 summarizes different constants that characterize the hydrogen permeation in Ni-Zn-P, Zn-Ni and Cd coated steel. The data shown for Cd deposited steel has been taken from our previous work [60]. The thickness of the coating was assumed to be negligible when compared to the thickness of the steel membrane. Thus, any effect of the coating on the diffusion of hydrogen is neglected. The accuracy of the computed values of transport and kinetic properties are primarily dependent on the accuracy of the diffusivity value [62]. Hence, a diffusion coefficient value of 2.67×10^{-7} cm^2/sec was used in these calculations [62]. As seen from the table, the i_0 value was the highest in case of Zn-Ni coated steel, when compared to those of Ni-Zn-P and Cd coated steel. Zn-Ni alloy has a high concentration of Zn that makes the corrosion potential more negative (-1.083 V vs. SCE), thus making the alloy susceptible to high hydrogen evolution [61]. However, in the case of Ni-Zn-P alloy, the Zn content in the alloy is reduced to 16.2-wt% and the corrosion potential shifts to a more positive value of –0.652 V vs. SCE. This also causes the observed decrease in the exchange current density indicating slower discharge kinetics of

hydrogen evolution for Ni-Zn-P alloys. Comparison of the adsorption-absorption coefficient shows that k'' was the largest for Cd coated steel followed by Zn-Ni and Ni-Zn-P. However, there is a large increase in the value of recombination rate constant k_3 for Zn-Ni alloy, when compared to Ni-Zn-P and Cd. However, the large adsorption-absorption rate constant for Zn-Ni alloys counters the effect due to the increased recombination rate constant and hence the observed hydrogen permeation is the highest for Zn-Ni alloy. For Cd, even though the exchange current density for hydrogen evolution is the lowest among the three coatings, the large adsorption-absorption rate constant and low value of recombination rate constant ensures that most of the evolved hydrogen permeates into the substrate. However, Ni-Zn-P alloy combines the advantage seen in both these coatings - it exhibits low exchange current density and at the same time has high recombination rate constant. Such a favorable combination of these properties in the case of Ni-Zn-P alloys enables it to allow lower amount of hydrogen to permeate into the substrate than Zn-Ni and Cd coatings.

4. CONCLUSION

A mathematical model based on mixed potential theory was developed to explain the reactions happening during Ni-Zn-P deposition process. The concentrations of the Zn and Ni complex species for the model were obtained by solving the material balances in addition to the electroneutrality condition and equilibrium relations. Based on the model, it was seen that adsorption plays a significant role in the deposition process and controls the rate of deposition. It was also seen that addition of Zn ions to the bath inhibits the deposition rate by changing the coverages for the adsorbed reactants on the electrode surface. It was also experimentally confirmed that the addition of Zn ions to the bath increases the polarization resistance, thereby decreasing the plating rate. The composition of the coating was obtained by obtaining the partial current densities for the deposition reactions of Ni, Zn and P. The effect of pH on the deposition process was also studied. It was seen that the increase in pH increases the deposition rate for the process. The results obtained from the model agree very well with the experimental observations, validating the mechanism assumed in the mathematical model.

Composite Ni-Zn alloys with different amounts of Zn were prepared by controlling the deposition parameters such as applied potential, pH and amount of $ZnSO_4$ in the bath. Material characterization studies on the resultant coatings showed the co-deposition of Zn and Ni. The Zn content in the alloy can be controlled by varying the applied potential, Zn^{2+} concentration in the bath or by adjusting the bath pH. Electrochemical characterization studies reveal that composites with 28-wt% Zn have rest potential more electronegative to steel and hence are applicable as a sacrificial coating for the protection of steel. This optimal Zn content in the alloy is obtained when deposition with a $ZnSO_4$ concentration of 15 g/L, at pH 10.5 and 60 °C. The high Ni content (72-wt%) ensures the superior corrosion resistance of the composite alloy as compared to conventional Zn-based coatings obtained by electrolysis. Polarization resistance studies reveal a five-time increase in the resistance value for the Ni-Zn coating over that of Cd. The low potential difference that exists between the coating and the substrate results in a lower dissolution rate for the deposited alloy as compared to Zn, Zn-Ni and Cd coatings. Owing to its excellent corrosion properties, this new non-anomalous Ni-Zn alloy can be considered as an ideal replacement for cadmium coatings.

A novel electroplating process has been devised to obtain corrosion resistant Zn-Ni-Cu coatings. It has been shown that use of a ternary alloying element like $CuSO_4$ in small amounts can alter the Zn:Ni ratio in the deposit. Material characterization studies performed on the resulting deposits showed the codeposition of Cu along with Zn and Ni. Increasing the stirring speed increases the Cu and Zn content in the deposit with a decrease in the Nickel content. This is attributed to the kinetics of the deposition process; Cu and Zn deposition are diffusion limited while Nickel deposition is a kinetically limited process. The observed decrease in the nickel content arises out of the increase in the mass transfer limited Cu and Zn reduction processes. Beyond a concentration of 1 g/L of $CuSO_4$, Cu deposition dominates the whole process. With the use of 1 g/L of $CuSO_4$, a corrosion resistant Zn-Ni-Cu deposit with a Zn:Ni ratio of 1.3:1 and corrosion potential of –0.69 V was obtained. Electrochemical Impedance Spectroscopy and polarization studies show the corrosion resistance of this sacrificial coating is nearly five times that of the conventional Zn-Ni alloy. This increased corrosion resistance is attributed to the barrier properties arising from the higher nickel content in the deposit. The new Zn-Ni-Cu alloy deposited shows increased corrosion resistance and barrier properties in comparison with conventional Zn-Ni and Cd coatings.

The hydrogen permeation characteristics of Ni-Zn-P coated steel was evaluated under cathodically polarized conditions and was compared with those of Zn-Ni and Cd coated steel. It was seen that Ni-Zn-P coating exhibits much lower permeation current density (0.64 $\mu A/cm^2$) than Zn-Ni (7.1 $\mu A/cm^2$) and Cd (2.2 $\mu A/cm^2$) coatings under similar conditions. To understand this reduction in permeation currents for Ni-Zn-P alloy, the experimental results were analyzed using the I-P-Z model to estimate the parameters that control hydrogen evolution and permeation kinetics. The surface hydrogen coverage remains low for Zn-Ni and Ni-Zn-P coatings, thus validating the assumption of Langmuir isotherm for hydrogen coverage and hence the use of I-P-Z model for data analysis. Analysis of the experimental data reveals that the adsorption-absorption constant is the highest for Cd coated steel, which indicates that the rate at which hydrogen is absorbed into the substrate is the highest in Cd coating. Even though Zn-Ni coating has the highest recombination constant among the three alloys, the high hydrogen evolution current density and the high absorption-adsorption constant still makes it susceptible to high hydrogen permeation as seen from the experimental results. It was seen that Ni-Zn-P alloy

combines the advantages seen in both Zn-Ni and Cd coatings, i.e., have low exchange current density and high recombination constant ensuring most of the hydrogen that is adsorbed on the surface of Ni-Zn-P alloys recombines chemically, thus reducing to a large extent the hydrogen ingress into the substrate.

5. REFERENCES

[1] C.R.Tomachuk, C.M.de A.Freire, M.Ballester, R.Fratesi, G.Roventi, *Surf. Coat. Technol.,* **122,** 6 (1999).

[2] K. R. Baldwin, C. J. E. Smith, *Trans. of the Inst. of Met. Finish.,* **74,** 202 (1996)

[3] W. H. Safranek, *Plat. Surf. Finish.,* **84,** 45 (1997).

[4] A. Ashur, J. Sharon, I. E. Klein, *Plat. Surf. Finish.,* **83,** 58 (1996).

[5] A. J. Boehm, *Plat. Surf. Finish.*, **80**, 52 (1993).

[6] Y. P. Lin, J. R. Selman, *J. Electrochem. Soc.,* **140,** 1299 (1993).

[7] Y. Miyoshi, *J. ISIJ Int.,* **31,** 1 (1991).

[8] Y. H. Yau, S. G. Fountolakis, in *Proceedings of Zinc based Steel Coating Systems: Metallurgy and Performance,* p.143 Minerals, Metals and Materials Society, (1990).

[9] A. Shibuya, T. Kurimoto, K. Korekewa, K. Noti, *Tetsu-To-Hagane,* **66,** 71 (1980).

[10] N. Muira, T. Saito, T. Kanamaru, Y. Shindo, Y. Kitazawa, *Trans. Iron Steel Inst. Japan,* **23**, 913 (1983).

[11] M. R. Lambert, R. G. Hart, Paper # 860266, presented at the SAE meeting in Detroit, MI, Feb 24 (1986).

[12] *The Properties of Electrodeposited Metal and Alloy*, W. H. Safranek, Editor, p.466, AESF, Orlando, FL (1986).

[13] A. Brenner, *Electrodeposition of Alloys, Principles and Practice,* Chap. 1, Academic Press, New York (1963).

[14] N. S. Grigoryan, V. N. Kudryavtsev, P. A. Zhdan, I. Y. Kolotyrkin, E. A. Volynskaya, T. A. Vagramyan, *Zasch. Met.,* **25,** 288 (1989).

[15] D. E. Hall, *Plat. Surf. Finish.,* **70** , 59 (1983).

[16] K. Higaashi, H. Fukushima, T. Urakawa, T. Adaniya, K. Matsudo, *J.Electrochem. Soc.,* **128,** 2081 (1981).

[17] A. Krishniyer, M. Ramasubramanian, B. N. Popov, R. E. White, *Plat. Surf. Finish.,* **1,** 99 (1999).

[18] A. Durairajan, A. Krishniyer, B. N. Popov, B. Haran, R. E. White, *Corrosion,* **56**,283 (2000).

[19] Z. Zhou, T. J. O. Keefe, *Surf. Coat. Technol.*, **96**, 191 (1997).

[20] B. N. Popov, D. Slavkov, T. Grcev, Lj. Arsov, S.Kariavanov, *Kem. Ind.*, **1**,1(1986).

[21] B. N. Popov, M. Ramasubramanian, S. N. Popova, R. E. White, K. M. Yin, *J. Chem. Soc ., Faraday Trans.,* **92**, 4021 (1996).

[22] A. Durairajan, B. S. Haran, R. E. White, B. N. Popov, *J. Electrochem. Soc.,* **147**, 1781 (2000).

[23] A. Durairajan, B. S. Haran, R. E. White, B. N. Popov, *J. Electrochem. Soc.,* **147**, 4507 (2000).

[24] H. Kim, K. S. Chen, B. N. Popov, *J. Electrochem. Soc.,* **151**, B275 (2003).

[25] M. Bouanani, F. Cherkaoui, R. Fratesi, G. Roventi, G. Barucca, *J. Appl. Electrochem.,* **29,** 637 (1999).

[26] E. Valova, I. Georgiev, S. Armyanov, J.-L. Delplancke, D. Tachev, Ts. Tsacheva, J. Dille, *J. Electrochem. Soc.,* **148,** C266 (2001).

[27] M. Schlesinger, X. Meng, D. D. Snyder, *J. Electrochem. Soc.,* **138,** 406 (1991).

[28] B. Veeraraghavan, S. P. Kumaraguru, B. Haran, B. Popov, *J. Electrochem. Soc.,* **150,** B151 (2003).

[29] B. Veeraraghavan, H. Kim, B. Haran, B. Popov, *Accepted for Publication in Corrosion.*

[30] M. Paunovic, *Plating,* **55,** 161 (1968).

[31] F. M. Donahue, *J. Electrochem. Soc.,* **119,** 72 (1972).

[32] P. Bindra, J. Roldan, *J. Appl. Electrochem.,* **17,** 1257 (1987).

[33] I. Ohno, M. Suzuki, S. Haruyama, *Proceedings of the 1st AESF Electroless Plat. Symp.*, Paper 16, 12 pp. (1982).

[34] M. Ramasubramnian, B. N. Popov, R. E. White, K. S. Chen, *J. Electrochem. Soc.,* **146,** 111 (1999).

[35] L. M. Abrantes, J. P. Correia, *J. Electrochem. Soc.,* **141,** 2357 (1994).

[36] M. Paunovic, M. Schlesinger, *Fundamentals of Electrochemical Deposition,* Chap. 8, John Wiley & Sons, New York (1998).

[37] Y. S. Kim, H. J. Sohn, *J. Electrochem. Soc.,* **143,** 505 (1996).

[38] G. Roventi, R. Fratesi, R. A. Della Guardia, G. Abrucca, *J. Appl. Electrochem.*, **30,** 173 (2000).

[39] W. M. Latimer, *Oxidation states of the elements and their potentials in aqueous solutions,* Prentice-Hall Inc., New York (1952).

[40] M. Wasberg, G. Horanyi, Electrochim. Acta., **40**, 615 (1995).

[41] M. Pourbaix, *Atlas of Electrochemical Equilibria in Aqueous Solutions,* Permagon Press, New York (1966).

[42] F. J. Fabri Miranda, O. E. Barcia, O. R. Mattas, R. Wiart, *J. Electrochem. Soc.*, **144**, 3449 (1997).

[43] V. G. Roev , N. V. Gudin, *Rus. J. Electrochem. Soc.*, **32**,325 (1996).

[44] S. Chen, *A Mathematical Model for the Electrodeposition of Amorphous Alloys on a Rotating Disk Electrode, M. S. Thesis,* Department of Chemical Engineering, Texas A&M University, Texas (1986).

[45] I. Epelboin, M. Ksouri, R. Wiart, *J. Electrochem. Soc.*, **122**,1206 (1975).

[46] B. E. Wilde, T. Shimada, *Scripta Metall.*, **22**, 552 (1988).

[47] P. J. Grobner, D. L. Sponseller, D. E. Diesburg, *Corrosion,* **35**, 240 (1979).

[48] M. Manohar, *Ph.D. Thesis*, The Ohio State University, Columbus, OH (1990).

[49] B. E. Wilde, L. Chattoraj, *Scripta Metall.*, **26**, 627 (1992).

[50] K. R. Baldwin, C. J. E. Smith, *Trans. Inst. Met. Finish.*, **74**, 202 (1996).

[51] J. M. Chen, J. K. Wu, *Plat. Surf. Finish.*, **33,** 657 (1992).

[52] M. Zamanzadeh, A. Allam, C. Kato, B. Ateya, H. W. Pickering, *J. Electrochem. Soc.*, **129,** 284 (1982).

[53] J. McBreen, L. Nanis, W. Beck, *J. Electrochem. Soc.*, **113**, 1218 (1966).

[54] B. S. Chaudhari, T. P. Radhakrishnan, *Surf. Technol.*, **22,** 353 (1984).

[55] S. K. Yen, H. C. Shih, *J. Electrochem. Soc.*, **135**, 1169 (1988).

[56] R. N. Iyer, H. W. Pickering, M. Zamanzadeh, *J. Electrochem. Soc.*, **136,** 2463 (1989).

[57] R. N. Iyer, I. Takeuchi, M. Zamanzadeh, H. W. Pickering, *Corrosion,* **46,** 460 (1990).

[58] M. Ramasubramanian, B. N. Popov, and R. E. White, *J. Electrochem. Soc.*, **145,** 1907 (1998).

[59] M. A. V. Devanathan, Z. Stachurski, *J. Electrochem. Soc.*, **110,** 886 (1963).

[60] H. Kim, B. Popov, K. S. Chen, *Accepted for publication in Corr. Sci.,* 2003.

[61] D. H. Coleman, G. Zheng, B. N. Popov, R. E. White, *J. Electrochem. Soc.,* **143,** 1871 (1996).

[62] A. Durairajan, *Ph.D. Thesis*, University of South Carolina, Columbia, SC (2001)

6. APPENDIX

The electroless bath used for deposition consists of 35 g/L $NiSO_4 \cdot 6H_2O$, 15 g/L $ZnSO_4 \cdot 7H_2O$, 85 g/L Sodium citrate and 50 g/L Ammonium chloride. The variables to be determined are as follows: $[Zn^{2+}]$, $[Ni^{2+}]$, $[Zn(OH)^{+}]$, $[Ni(OH)^{+}]$, $[Zn(OH)_2]$, $[Ni(OH)_2]$, $[Zn(NH_3)_4^{2+}]$, $[Ni(NH_3)_6^{2+}]$, $[Zn_2(OH)^{3+}]$, $[OH^{-}]$, $[SO_4^{2-}]$, and $[HSO_4^{-}]$. The concentration of $[H^{+}]$ depends on the specified pH. The equations used for the determination of the equilibrium concentrations are

Material balance on zinc

$$[ZnSO_4]_{ad} = [Zn^{2+}] + [Zn(OH)^{+}] + 2[Zn_2(OH)^{3+}] + [Zn(OH)_2] + [Zn(NH_3)_4^{2+}]$$

Material balance on nickel

$$[NiSO_4]_{ad} = [Ni^{2+}] + [Ni(OH)^{+}] + [Ni(OH)_2] + [Ni(NH_3)_6^{2+}]$$

Electroneutrality conditions

$$[H^{+}] + 2[Zn^{2+}] + 2[Ni^{2+}] + [Zn(OH)^{+}] + [Ni(OH)^{+}] + 3[Zn_2(OH)^{3+}]$$
$$+ 2[Zn(NH_3)_4^{2+}] + 2[Ni(NH_3)_6^{2+}] = [HSO_4^{-}] + 2[SO_4^{2-}] + [OH^{-}]$$

The equilibrium conditions

$$[H^{+}][SO_4^{2-}] - k_1[HSO_4^{-}] = 0$$

$$[Zn^{2+}][OH^{-}] - k_2[Zn(OH)^{+}] = 0$$

$$[Ni^{2+}][OH^{-}] - k_3[Ni(OH)^{+}] = 0$$

$$[H^{+}][OH^{-}] - k_4 = 0$$

$$[Zn^{2+}]^2[OH^{-}] - k_5[Zn_2(OH)^{3+}] = 0$$

$$[Zn(OH)^{+}][OH^{-}] - k_6 = 0$$

$$[Ni(OH)^{+}][OH^{-}] - k_7 = 0$$

$$[Zn(OH)_2][NH_3]_{ad}^4 - k_8[Zn(NH_3)_4^{2+}][OH^{-}]^2 = 0$$

$$[Ni(OH)_2][NH_3]_{ad}^6 - k_9[Ni(NH_3)_6^{2+}][OH^{-}]^2 = 0$$

The above equations were solved simultaneously by using Maple®. The various rate constants used in the equations are as follows: k_1=1.2 x 10^{-2} mol/L, k_2=1.1 x 10^{-6} mol/L, k_3=2.0 x 10^{-5} mol/L, k_4=1.0 x 10^{-14} mol^2/L^2, k_5=5.1622 x 10^{-8} mol^2/L^2, k_6=1.3 x 10^{-16} mol^2/L^2, k_7=6.3 x 10^{-16} mol^2/L^2, k_8=2.1 x 10^{7} mol^2/L^2 and k_9=1.7 x 10^{6} mol^2/L^2.

7. TABLES

Table 1. Experimental Conditions used in the study

Composition of Electrolyte (g/L)	
$NiSO_4.6H_2O$	35
$ZnSO_4.7H_2O$	5-20
Sodium Citrate	85
NH_4Cl	50
Sodium Hypophosphite	20
Experimental Conditions	
Angular velocity, ω	400 rpm
Radius of the disk electrode, r	0.25 cm
Kinematic viscosity, υ	0.012 cm^2/s
pH	10.5
Temperature	85 °C

Table 2. Kinetic Parameters used in the model

Kinetic Parameters	$H_2PO_2^-$ (anodic)[a]	$H_2PO_2^-$ (cathodic)[a]	$Ni(NH_3)_6^{2+}$ (cathodic)[b]	$Zn(NH_3)_4^{2+}$ (cathodic)[d]	H^+ (cathodic)[b]
Diffusion co-efficient, D (cm^2/s)	1.7×10^{-5}	1.7×10^{-5}	0.5×10^{-6}	5.0×10^{-6}	4.5×10^{-5}
Exchange current density, i_0 (A/cm^2)	7.0×10^{-6}	2.0×10^{-3}	7.5×10^{-4} [e]	7.5×10^{-3} [e]	1.5×10^{-5}
Anodic transfer co-efficient, α	0.5	0.5	0.8	0.5	0.7
Cathodic transfer coefficient, β	0.5	0.5	0.2	0.5	0.3
Number of electrons, n	2	1	2	2	2
Stability Constant, K_j (X 10^7 mol^2/L^2)	-	-	0.17 [d]	2.1 [d]	-

[a,b,c,d] Data obtained from literature [37,39,44,45].

[e] Parameter assumed in this model.

Table 3: Variation in Corrosion potential and Corrosion current density as a function of Zn content in the coatings.

Zn content in the deposit (wt %)	Corrosion potential E_{corr} (V vs. SCE)	Corrosion current density I_{corr} (A/cm^2)
0	-0.401	2.5×10^{-6}
28	-0.678	4.8×10^{-6}
31	-0.695	6.1×10^{-6}
40	-0.722	8.6×10^{-6}
52	-0.752	1.5×10^{-5}

Table 4: Corrosion properties of different sacrificial coatings determined by linear and tafel polarization studies

Coating	Composition (wt%)				E_{corr} (V vs. SCE)	I_{corr} (A/cm^2)	Corrosion rate (x 10^{-10} cm/s)
	Zn	Ni	P	Cd/Cu			
Zn	100	-	-	-	-1.123	1.5×10^{-3}	39.4
Zn-Ni	94.6	5.4	-	-	-1.083	3.8×10^{-4}	17.7
Cd	-	-	-	100	-0.798	9.5×10^{-5}	17.2
Zn-Ni-Cd	45	35		20	-0.692	1.0×10^{-5}	4.9
Ni-Zn-P	16.2	74.0	9.8	-	-0.652	8.5×10^{-6}	3.3
Ni-Zn	28.0	72.0	-	-	-0.678	4.8×10^{-6}	2.9

Table 5: Comparison of mechanical properties for the various sacrificial coatings

Coating	Adhesion	Taber Wear index (mg)	Micro-hardness (HK_{25})
Zn	Good	29.7	82
Zn-Ni	Mild flaking	18.5	105
Cd	Good	6.0	240
Ni-Zn-P	Good	8.0	198

Table 6: Kinetic parameters characterizing the hydrogen evolution and permeation through various coatings.

Deposit	i_0 (A/cm^2)	k^* (mol/cm^3)	k_3 (mol/cm^2-s)
Ni-Zn-P	4.69×10^{-7}	8.74×10^{-7}	1.06×10^{-8}
Cd	6.31×10^{-9}	7.32×10^{-5}	1.66×10^{-9}
Zn-Ni	4.03×10^{-5}	1.03×10^{-5}	1.15×10^{-6}

8. FIGURES

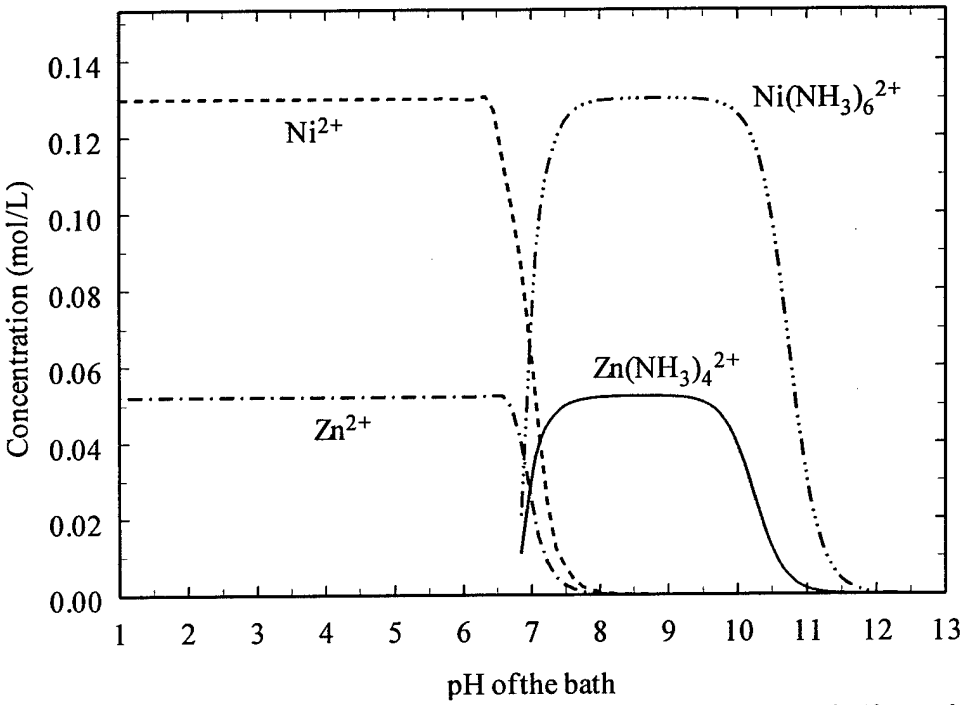

Figure 1: Variation in equilibrium concentrations of complexed Zn and Ni species as a function of bath pH.

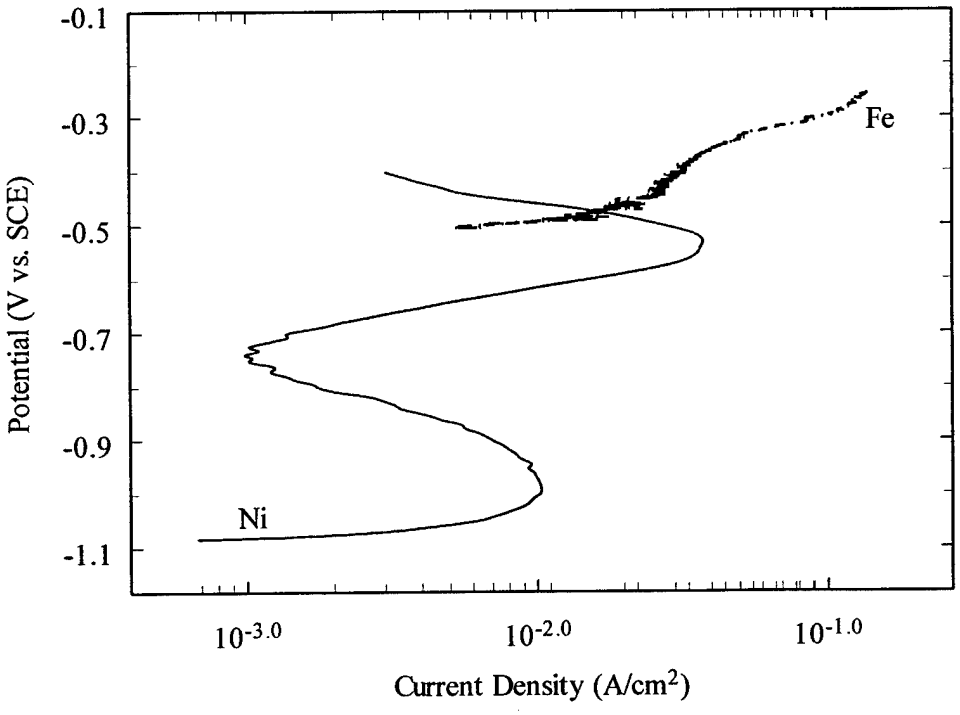

Figure 2: Polarization studies of hypophosphite oxidation on different substrates

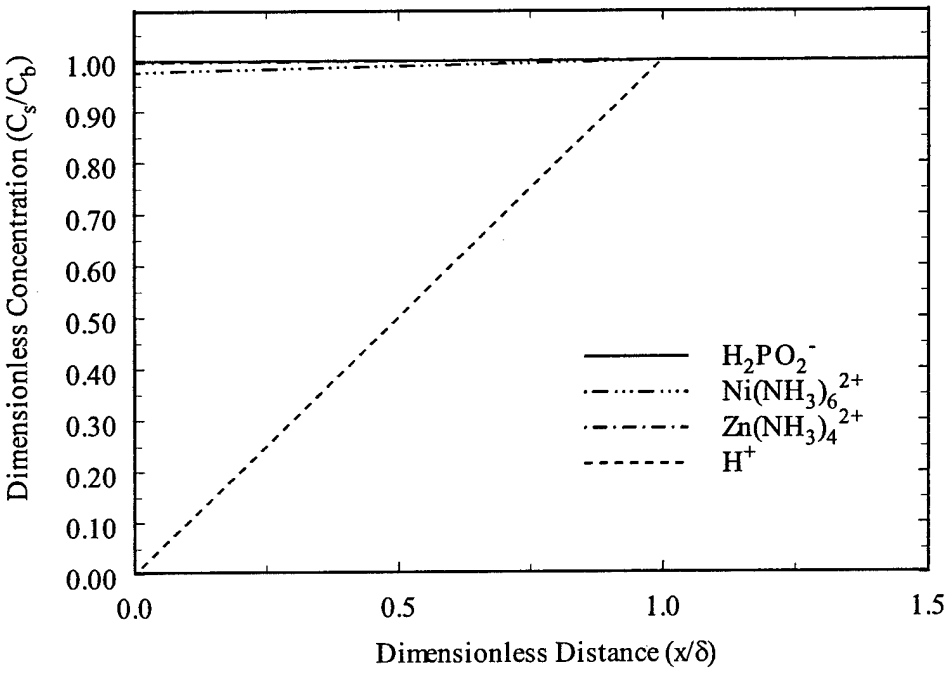

Figure 3: Dimensionless concentration profiles for the various reactants as a function of distance from the electrode surface.

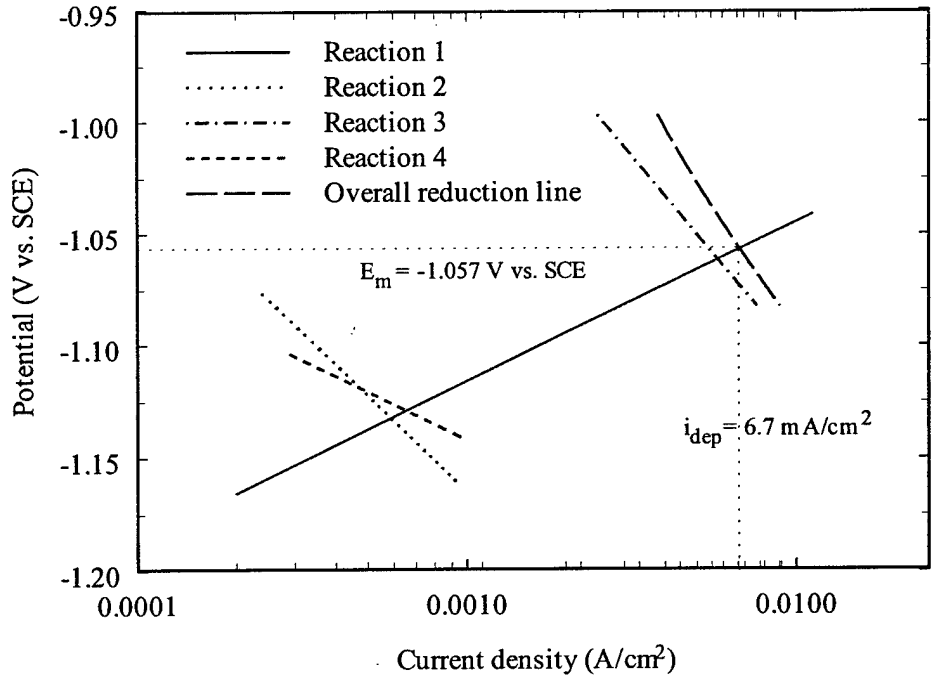

Figure 4: Evans diagram showing the various reactions happening during the electroless deposition process for a $ZnSO_4$ concentration of 5 g/L.

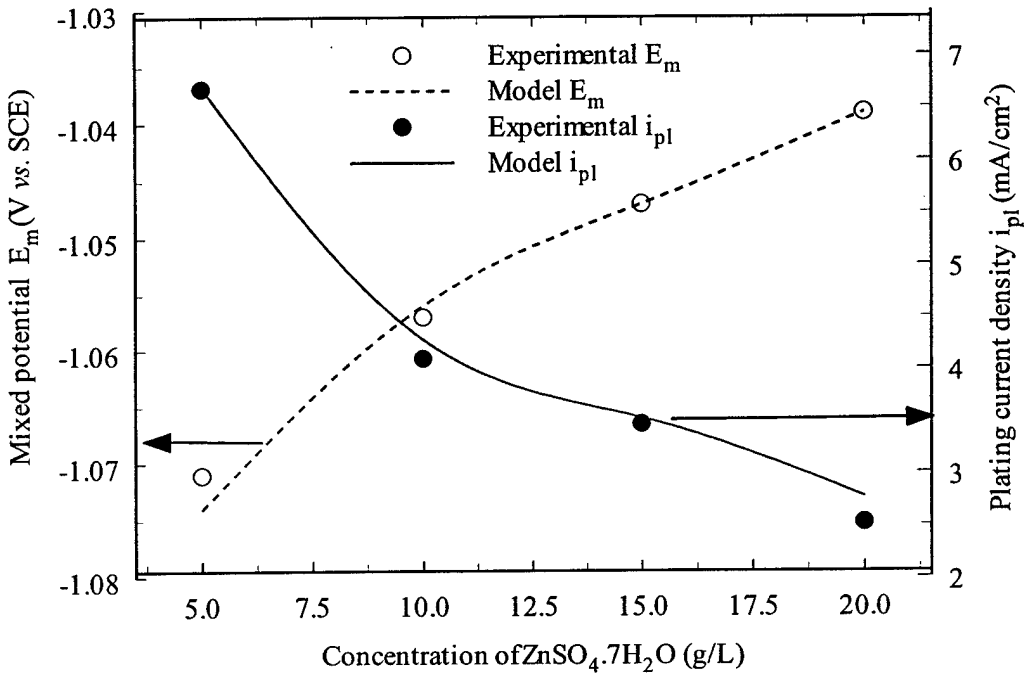

Figure 5: Comparison of mixed potential E_m and plating current density i_{pl} obtained from the model and the experiments as a function of $ZnSO_4$ concentration in the bath

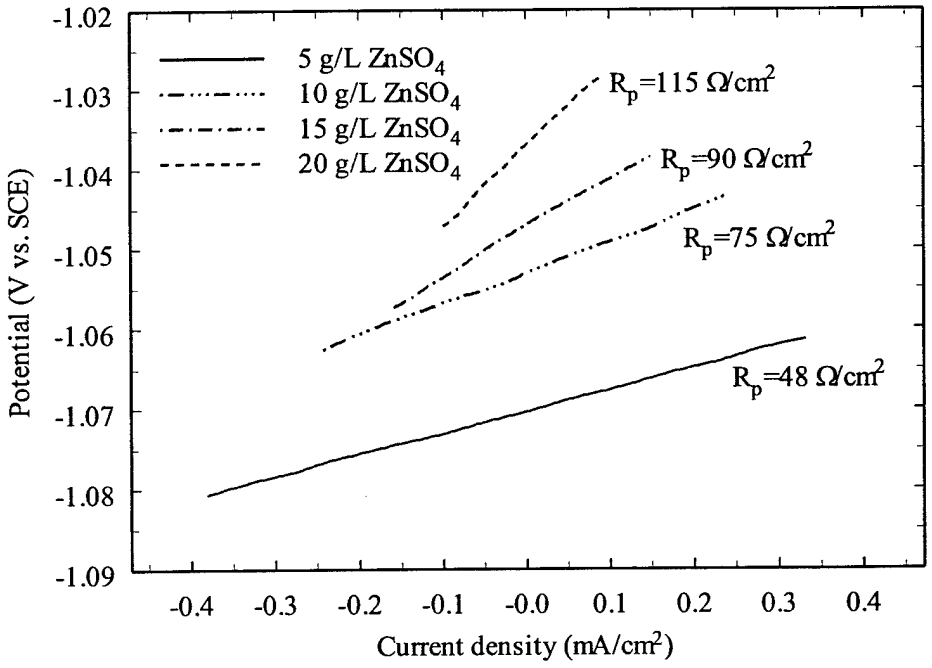

Figure 6: Linear polarization studies performed during the deposition process as a function of $ZnSO_4$ concentration in the bath

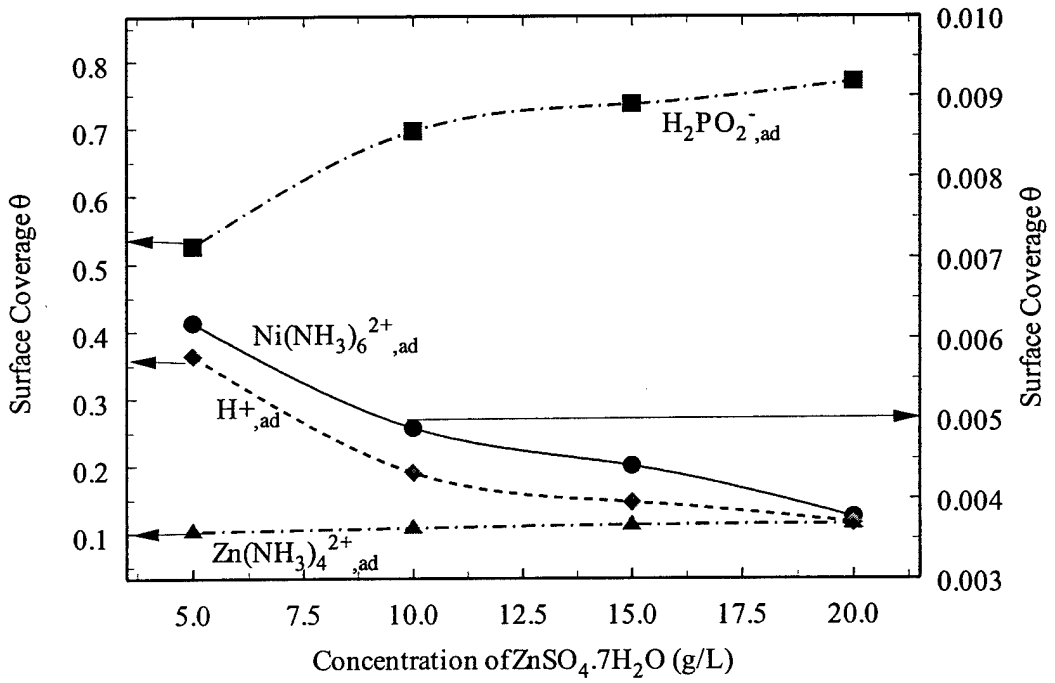

Figure 7: Variation in Surface Coverages of the different reacting species as a function of $ZnSO_4$ concentration in the bath

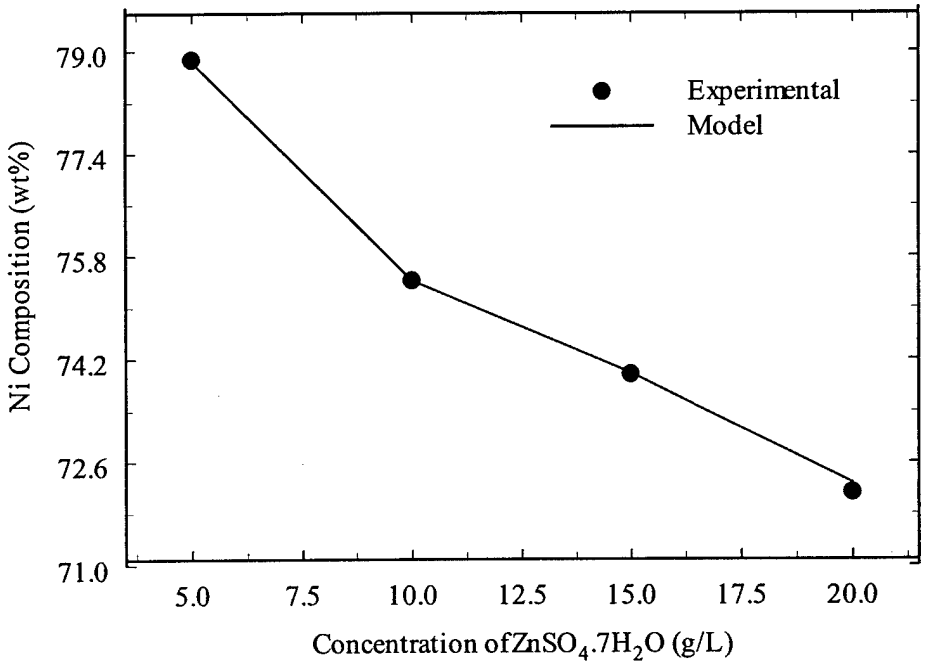

Figure 8: Variation in Ni content as a function of $ZnSO_4$ concentration in the bath.

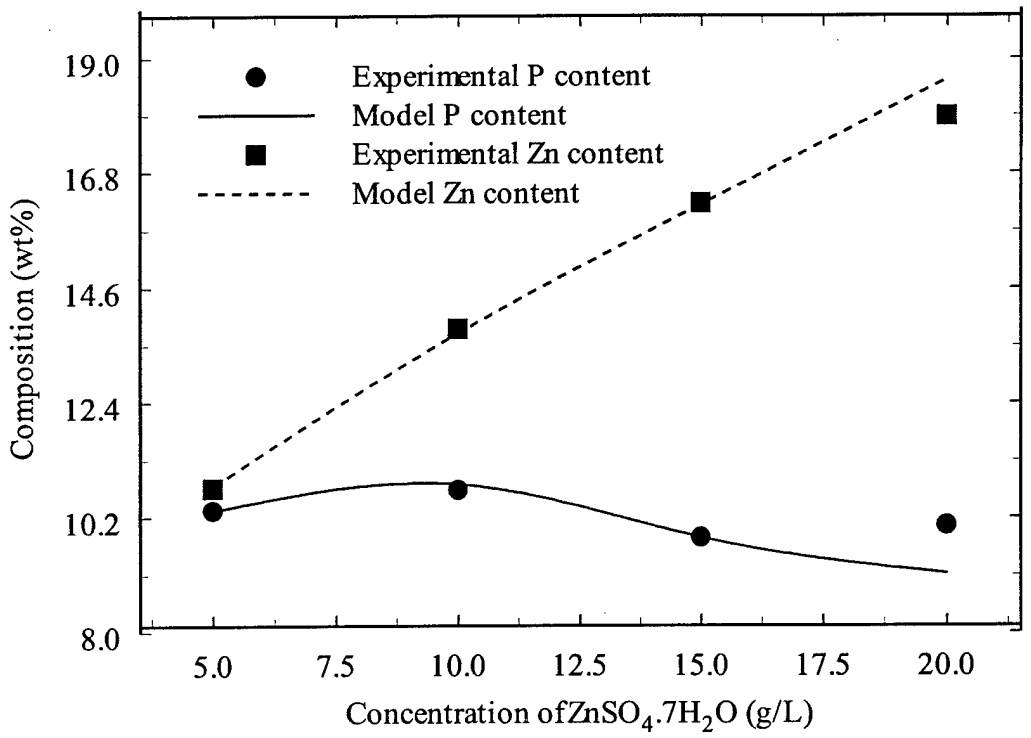

Figure 9: Variation in Zn and P content as a function of $ZnSO_4$ concentration in the bath.

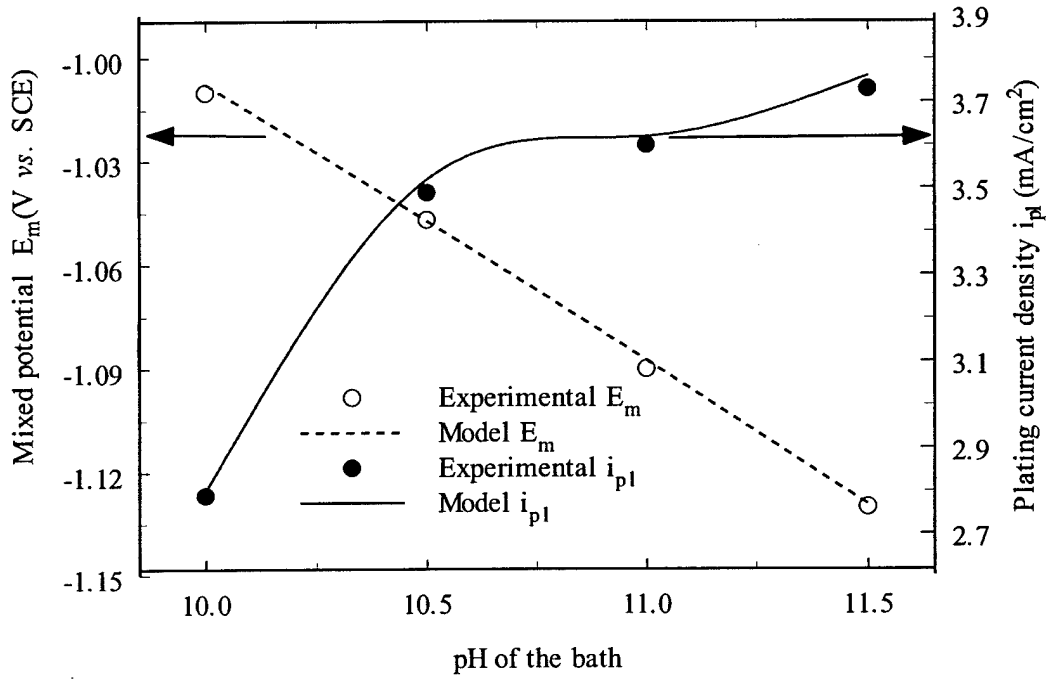

Figure 10a: Comparison of mixed potential E_m and plating current density i_{pl} obtained from the model and the experiments as a function of pH of the bath.

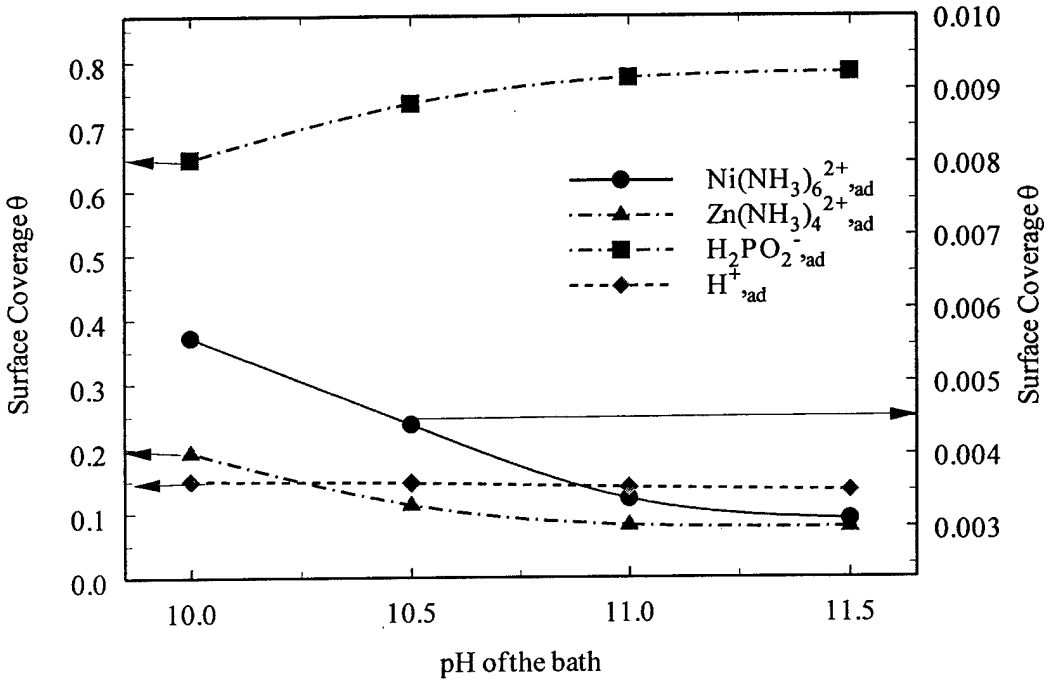

Figure 10b: Variation in Surface Coverages of the reacting species as a function of bath pH.

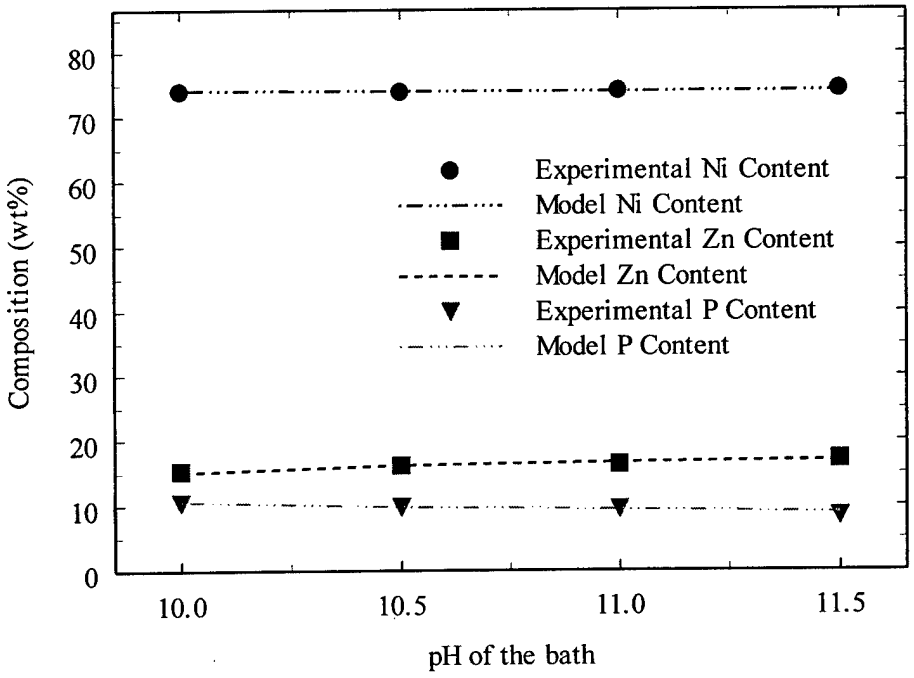

Figure 11: Comparison of Ni, Zn and P contents of the coating obtained from the model and the experiments as a function of pH of the bath.

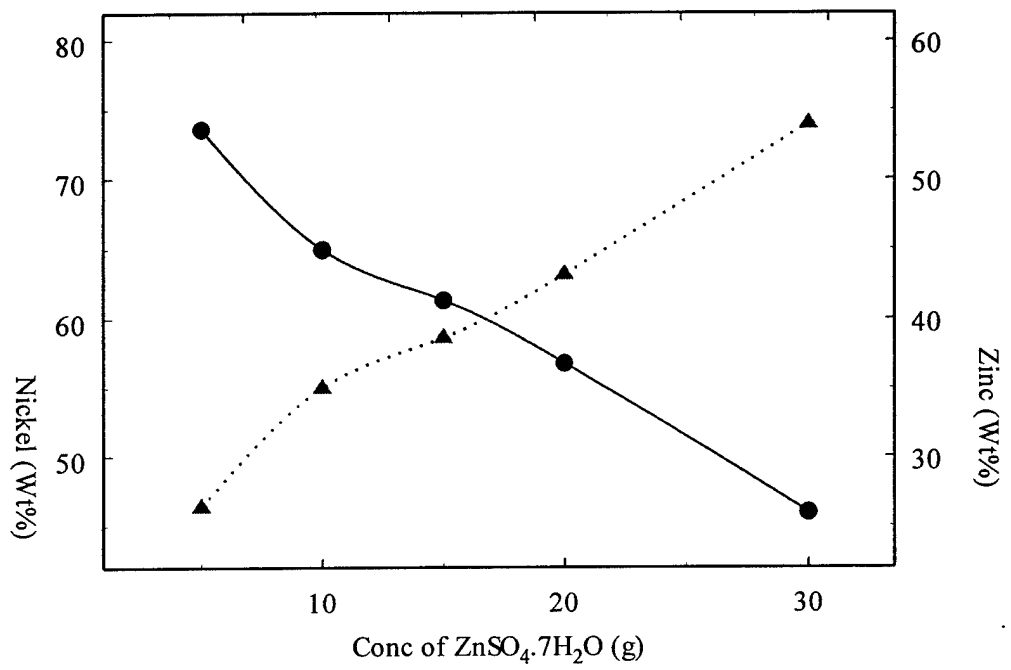

Figure 12: Variation in the composition of the coatings obtained as a function of $ZnSO_4.7H_2O$ concentration in the bath

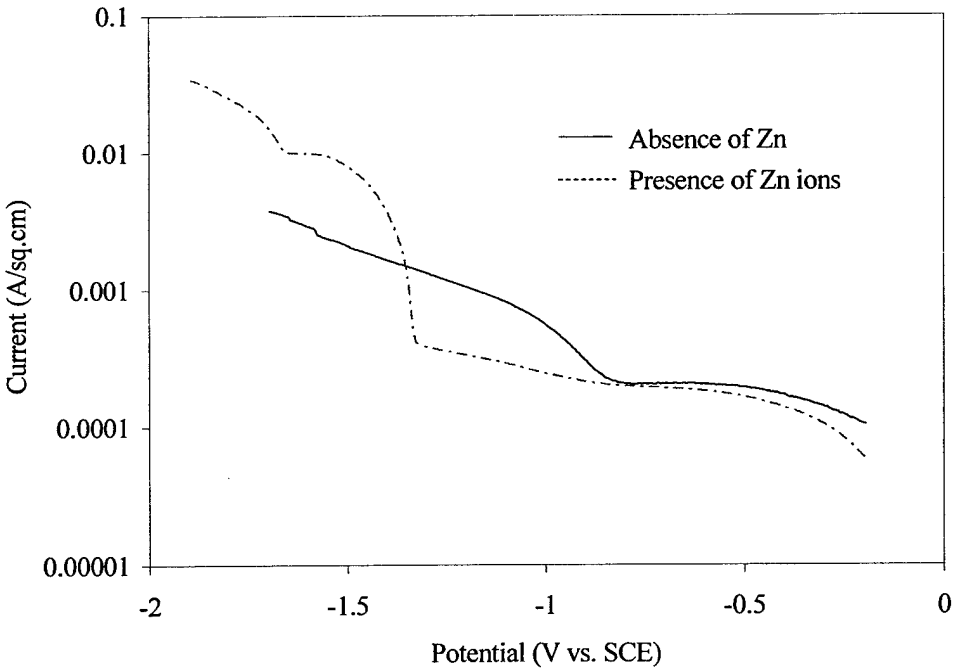

Figure 13a: Cathodic Polarization curves obtained from for the alkaline bath, in the absence of $NiSO_4.6H_2O$ and $ZnSO_4.7H_2O$ an in the presence of $ZnSO_4.7H_2O$

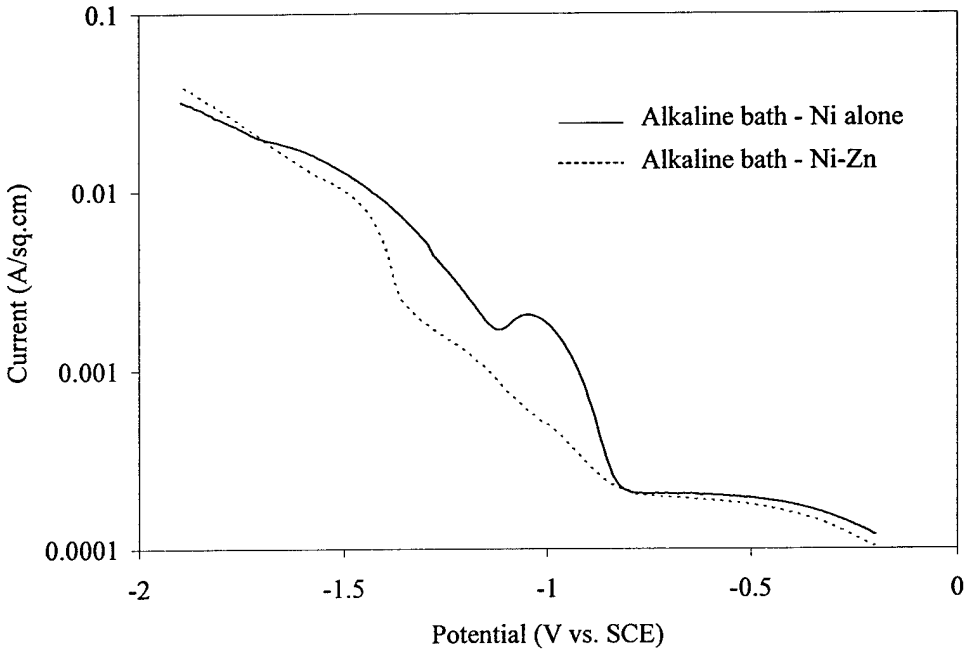

Figure 13 b: Cathodic polarization curves obtained from an alkaline the presence and absence of $ZnSO_4.7H_2O$.

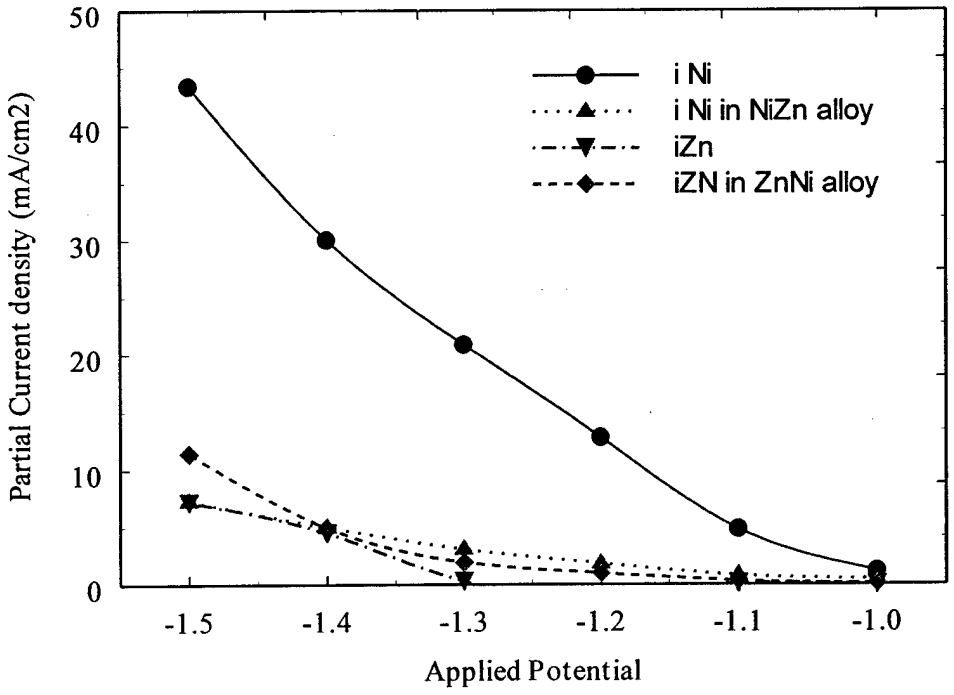

Figure 14: Partial current density of Ni and Zn in alloy and single metal deposition as a function of applied potential

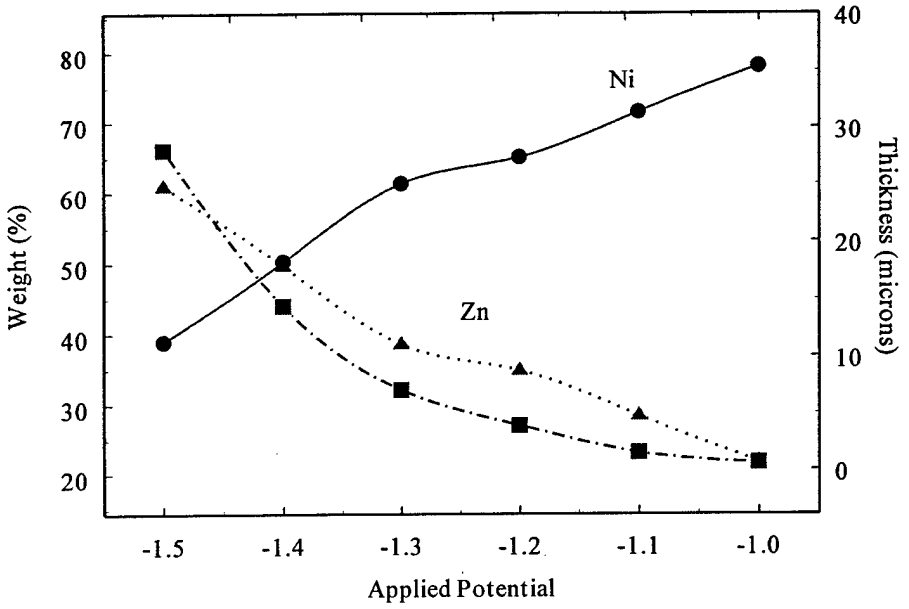

Figure 15: Variation in composition and thickness of the deposit as a function of the Applied potential

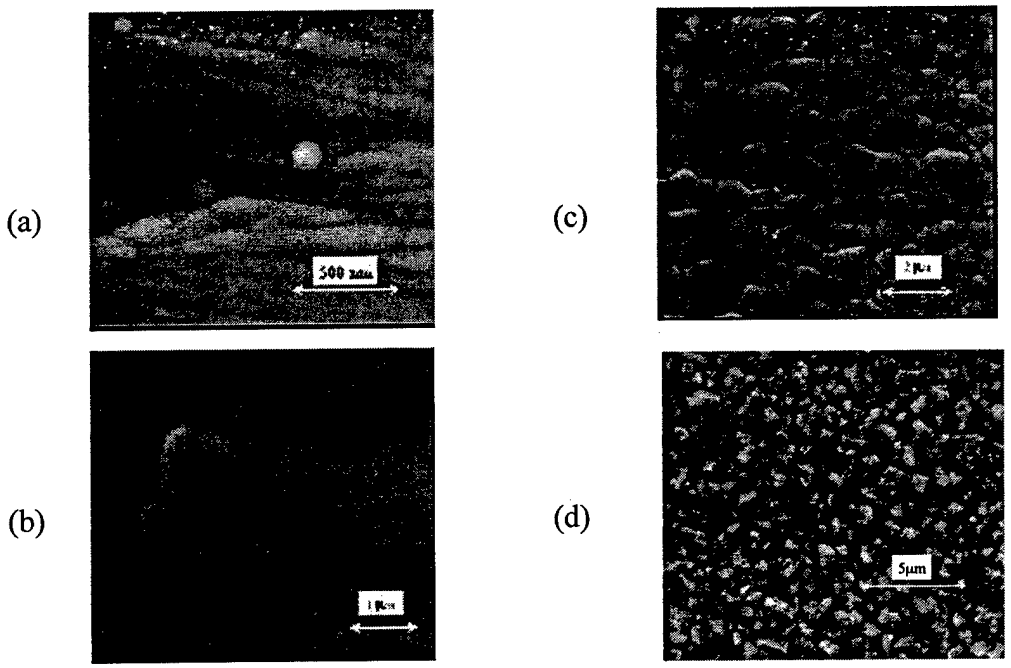

Figure 16: SEM Micrographs of N-Zn alloy deposited at (a) -1.0 V, (b)-1.1 V, (c) -1.3 V and (d) -1.5 V.

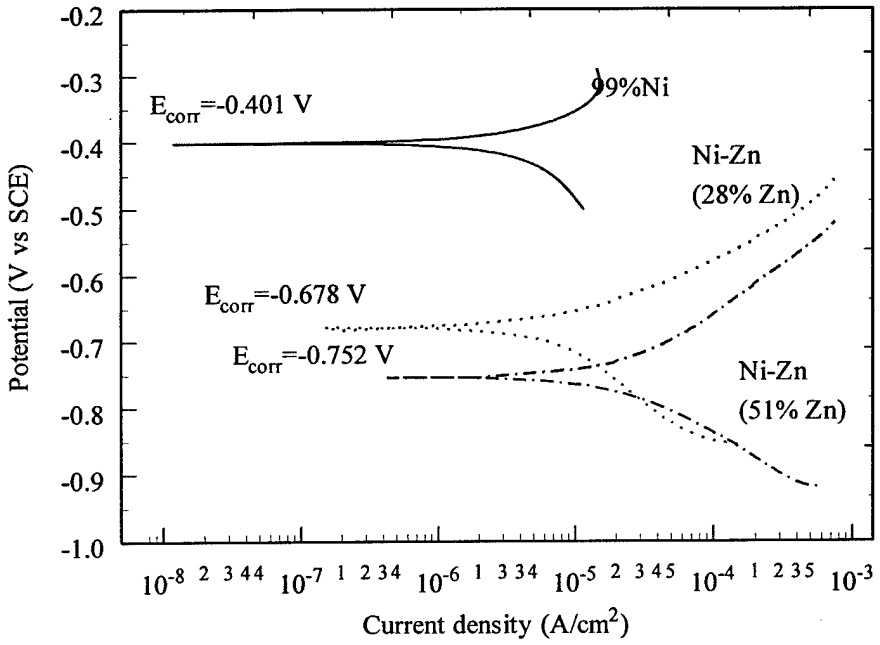

Figure 17: Tafel analysis of the Ni-Zn coatings as a function of Zn content in the final deposit. The corrosion potential becomes more electronegative as more Zn is included in the deposit

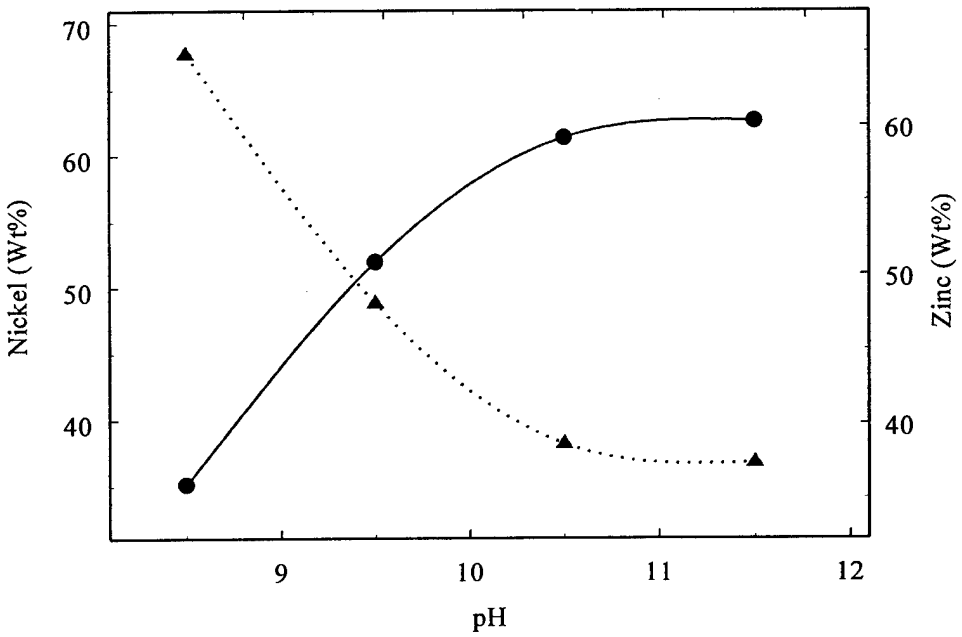

Figure 18: Variation in composition of the deposit as a function of the pH of the bath.

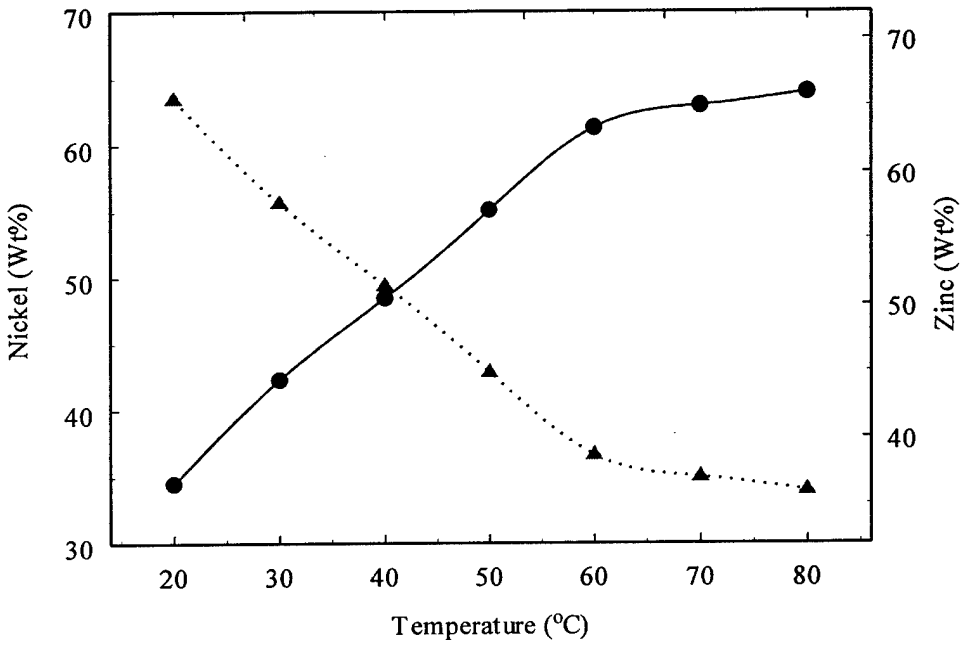

Figure 19: Variation in the composition of the deposit as a function of bath temperature.

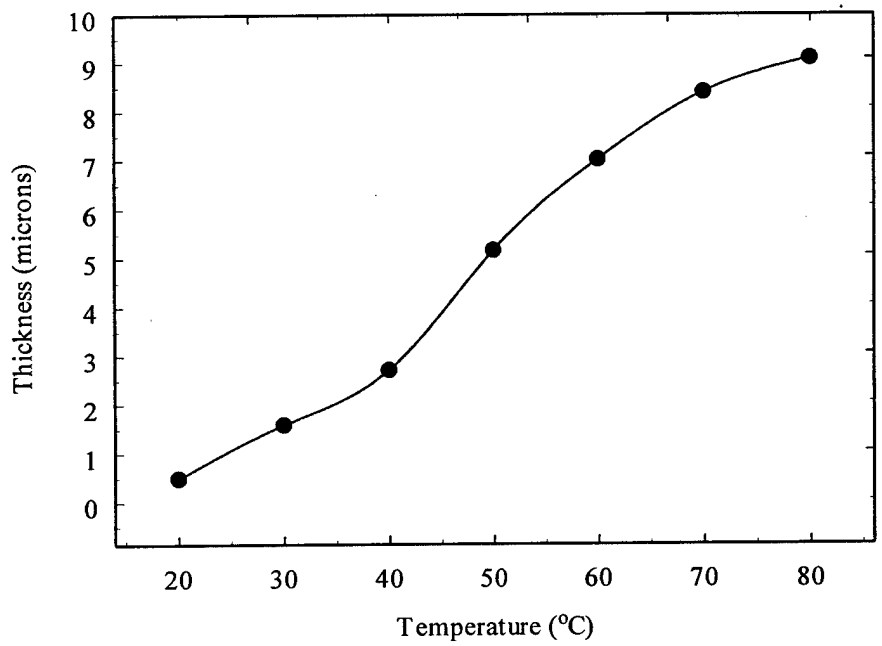

Figure 20: Variation in the deposition rate as a function of the bath temperature

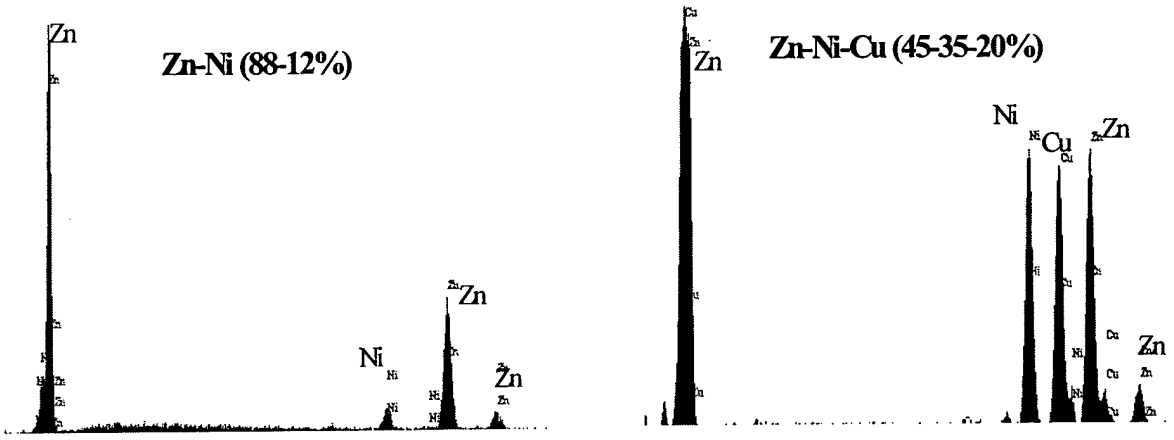

Figure 21: EDAX analysis of Zn-Ni alloy (88-12 %) and Zn-Ni-Cu alloy (45-35-20%).

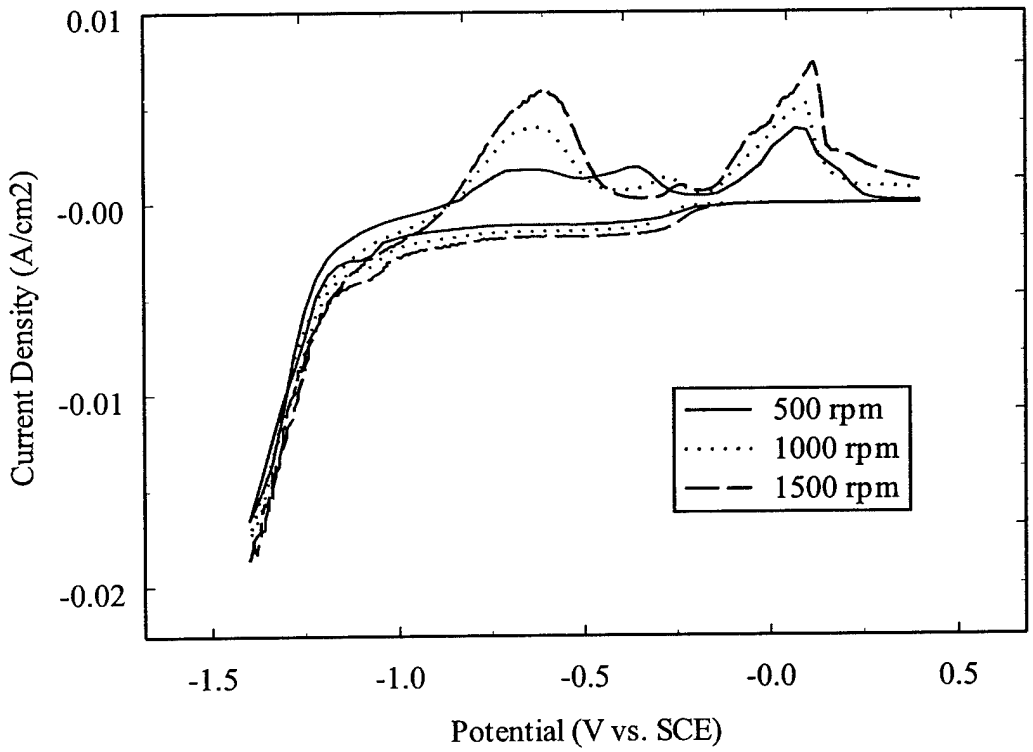

Figure 22: Cyclic voltammogram of Zn-Ni-Cu film electrodeposited from a solution of 40 g/L of NiSO4.6H2O, 20 g/L of ZnSO4 and 1 g/L of CuSO4 at a scan rate of 30 mV/s.

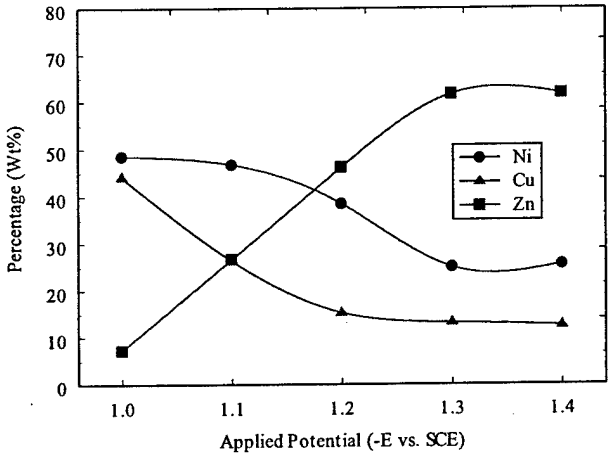

a) 0.5 g/L

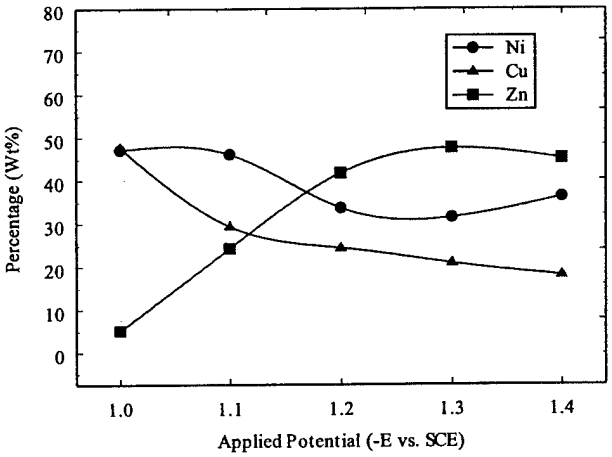

b) 1 g/L

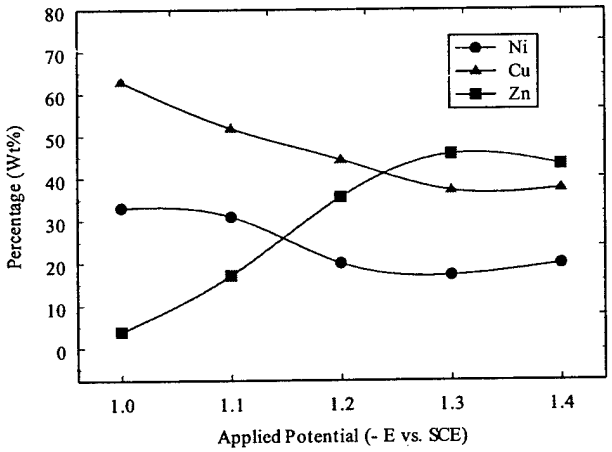

c) 2 g/L

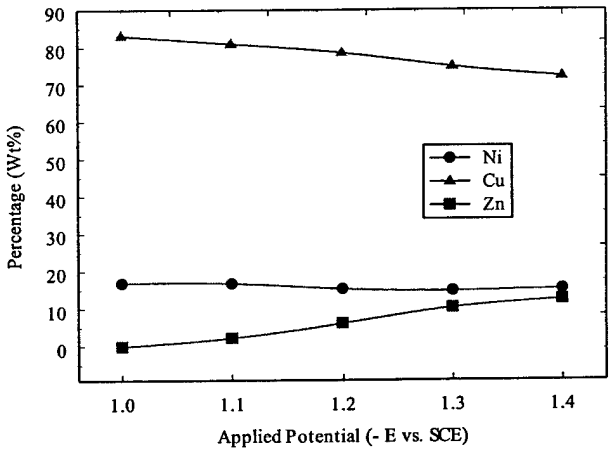

c) 4 g/L

Figure 23: Effect of $CuSO_4$ concentration on the alloy composition of electrodeposited Zn-Ni-Cu as a function of applied (negative) potential.

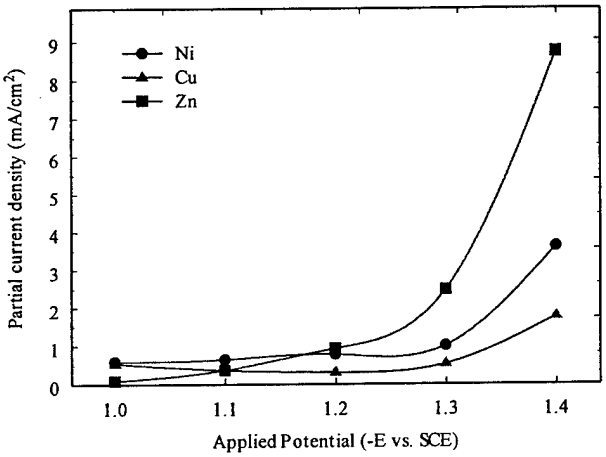

a) 0.5 g/L

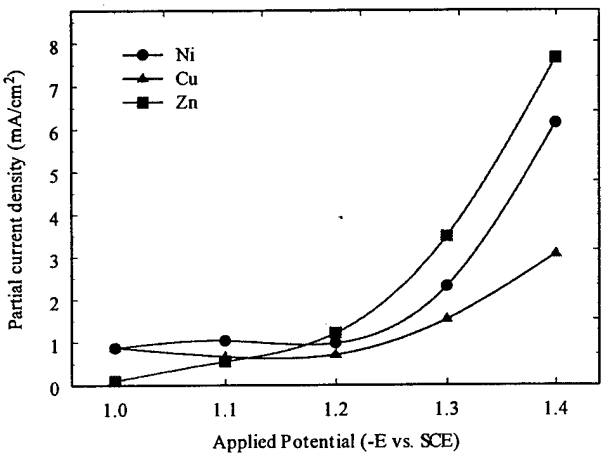

b) 1 g/L

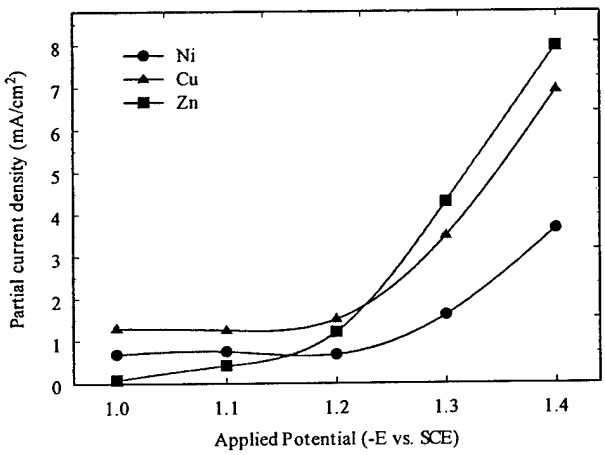

c) 2 g/L

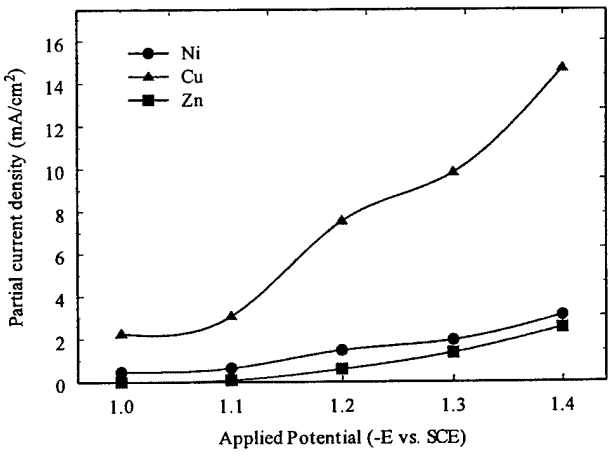

c) 4 g/L

Figure 24: Effect of $CuSO_4$ concentration on the partial current density of electrodeposited Zn-Ni-Cu as a function of applied (negative) potential.

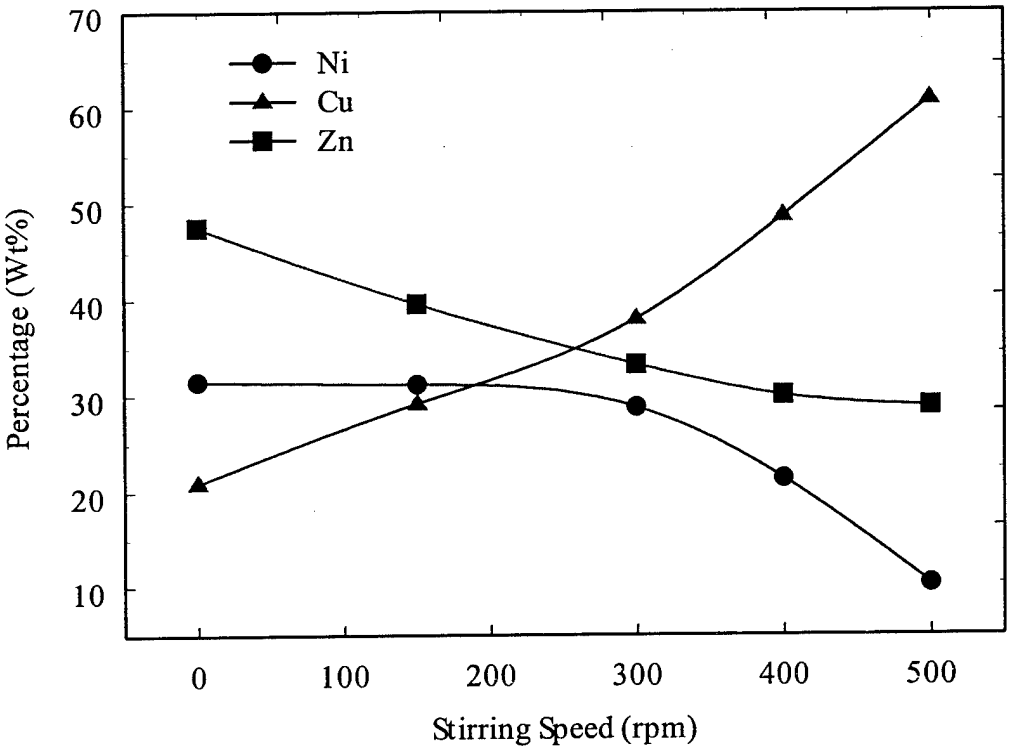

Figure 25: Effect of stirring on the composition of Zn-Ni-Cu alloy electrodeposited from 60 g/L of $NiSO_4.6H_2O$, 30 g/L of $ZnSO_4.7H_2O$ and 1 g/L of $CuSO_4$, pH 9.0 at -1.3 V (vs. SCE)

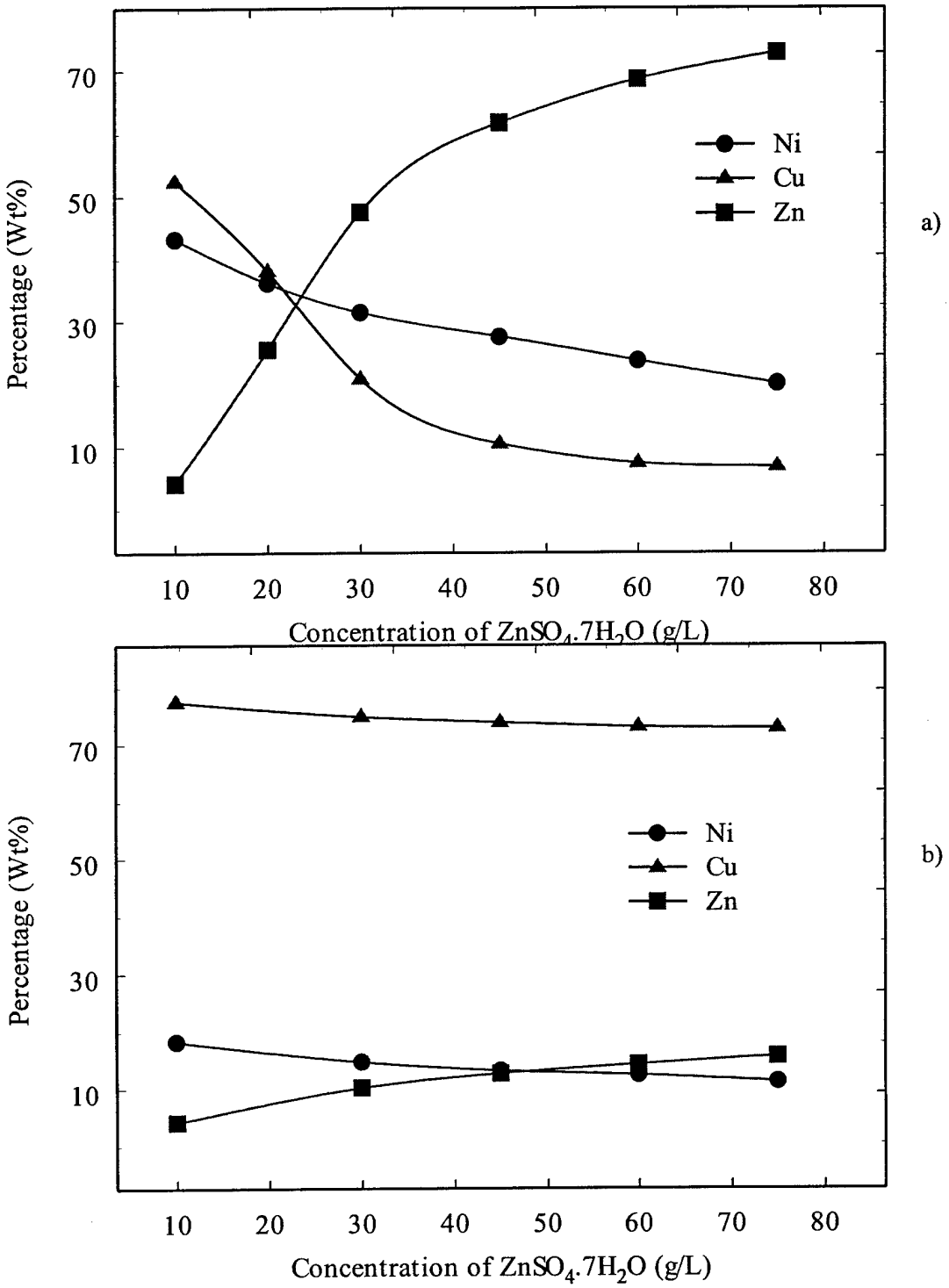

Figure 26: Effect of $ZnSO_4.7H_2O$ concentration on the composition of the Zn-Ni-Cu alloy electrodeposited from 60 g/L of $NiSO_4.6H_2O$, $ZnSO_4.7H2O$ in the presence of a) 1 g/L of $CuSO_4$, and b) 2 g/L of $CuSO_4$ pH 9.0 at -1.3 V (vs. SCE)

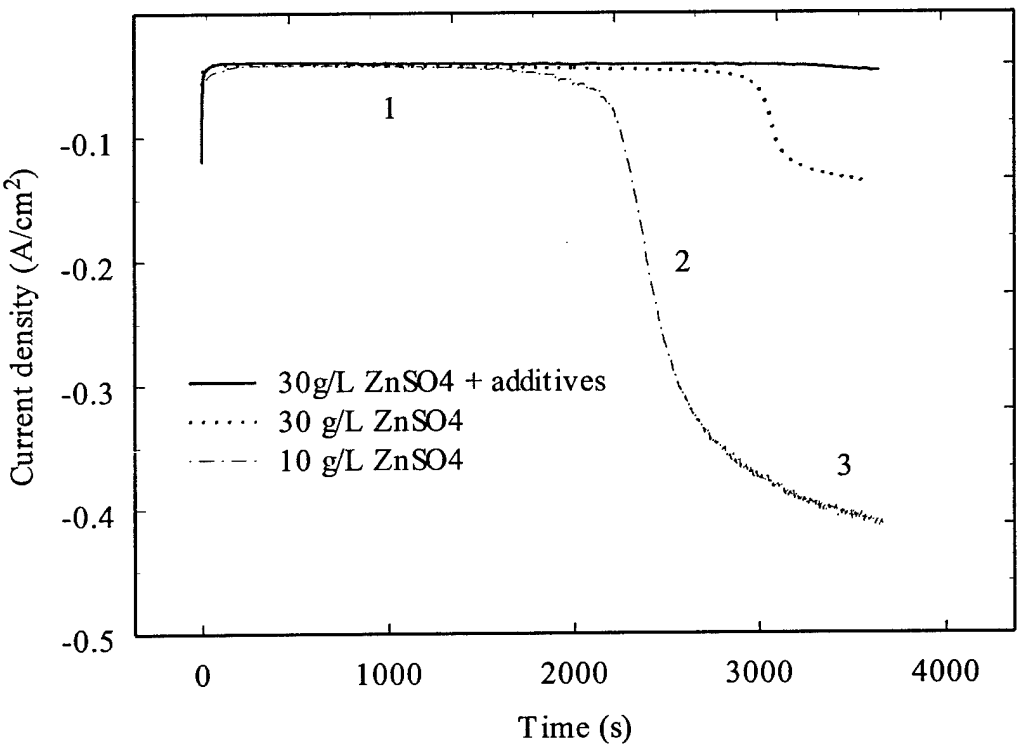

Figure 27 : Effect of ZnSO4 concentration and additive on the current density of deposition as a function of time.

1) 47/ 32/21

Zn/Ni/Cu

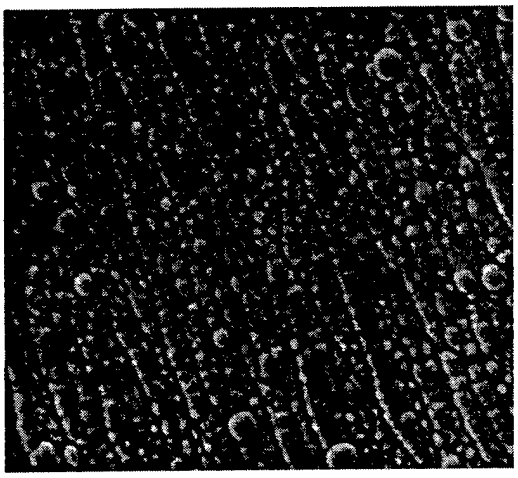

2) 18/42/40

Zn/Ni/Cu

47/32/21

Zn/Ni/Cu

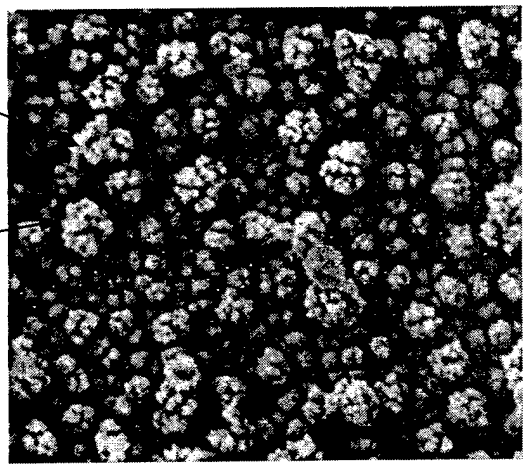

3) 28/37/35

Zn/Ni/Cu

Figure 28: Surface morphology of the coatings at the three points indicated in previous figure

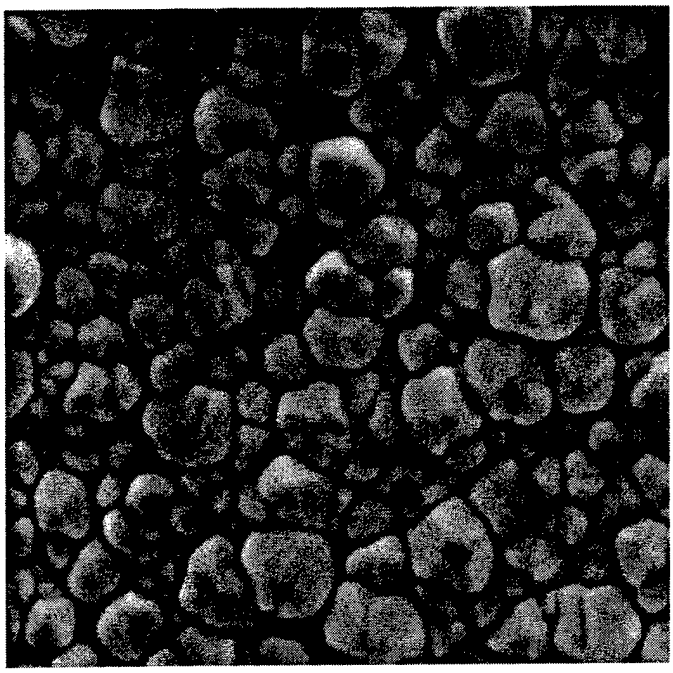

Figure 29: SEM micrograph of Zn-Ni-Cu deposit obtained from the bath containing additives, 0.5 g/L dextrin, and 60g/L of sodium citrate

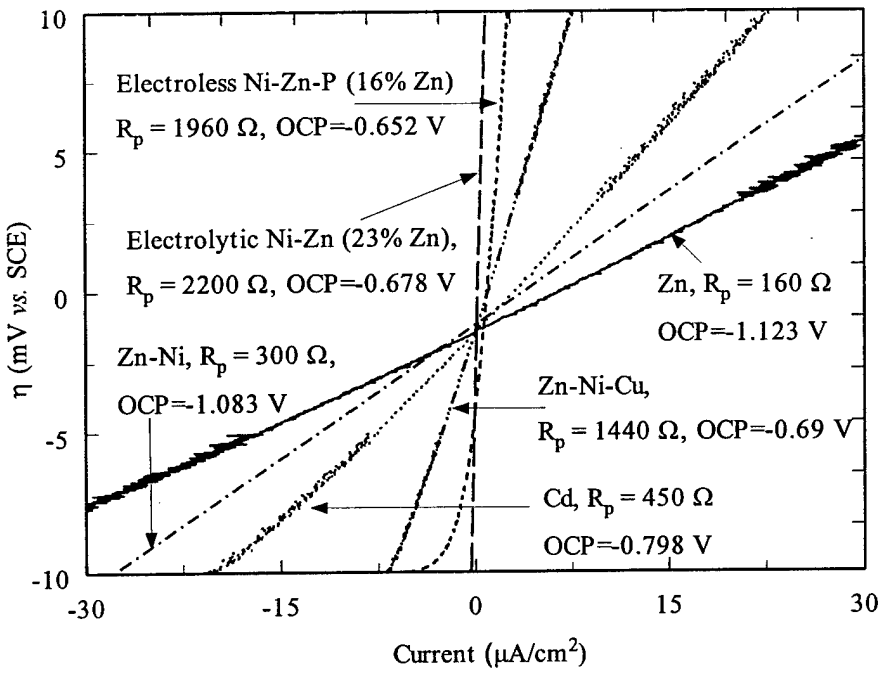

Figure 30a: Linear polarization plots for the various sacrificial coatings as compared with optimized Ni-Zn (28-wt% Zn) and Ni-Zn-P coatings. The graph shows a four-times increase in the polarization resistance for these coating as compared to Cd coating

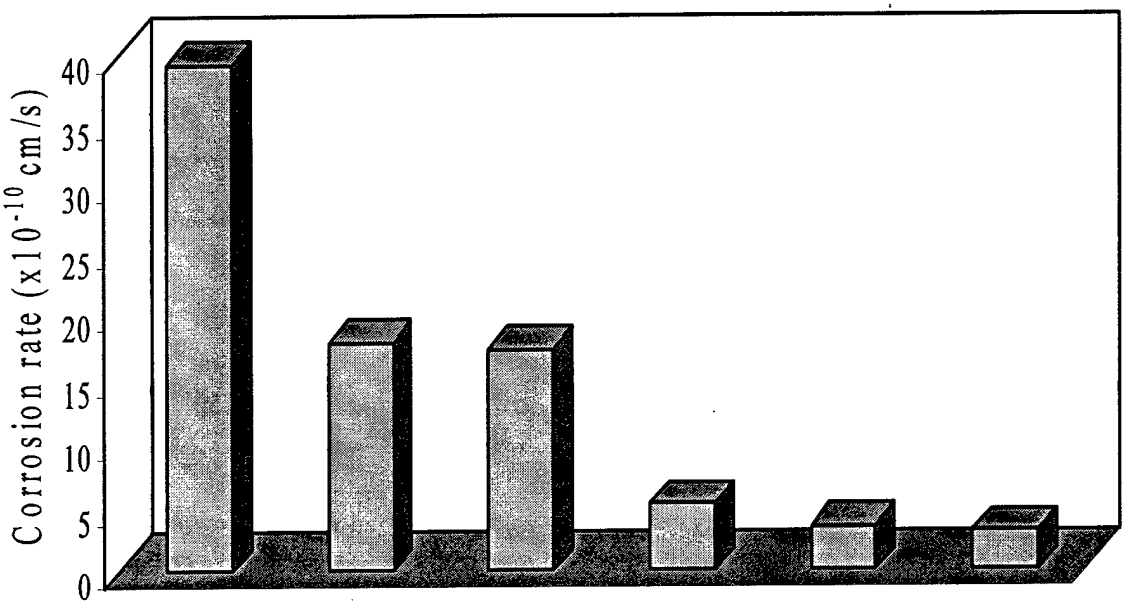

Figure 30b: Comparison of corrosion rates of various alloy coatings

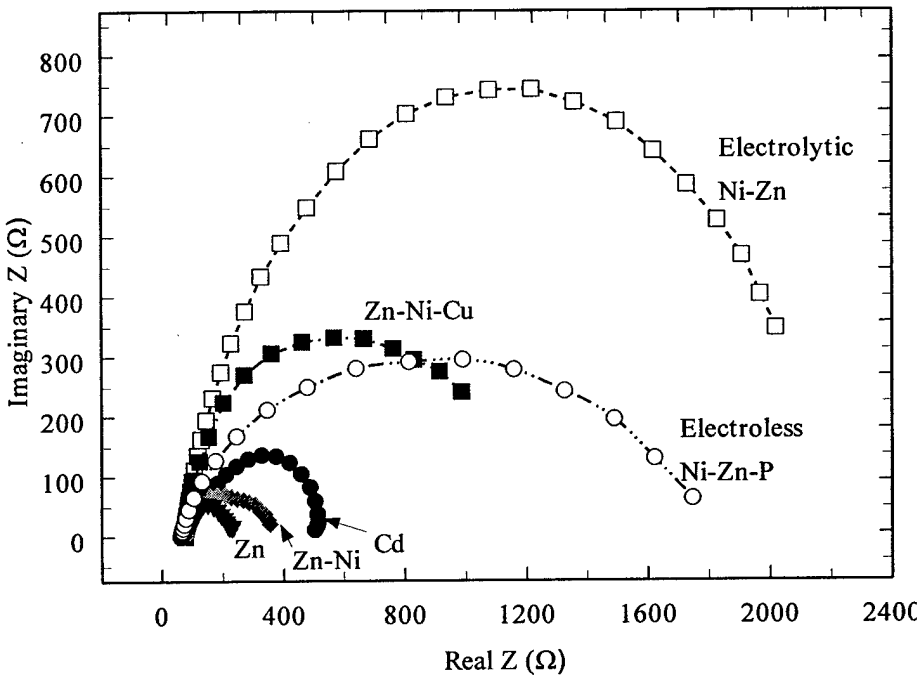

Figure 31: Nyquist plots obtained for various coatings in 71 g/L Na_2SO_4 and 30.5 g/L H_3BO_3 (pH=7.0) solution

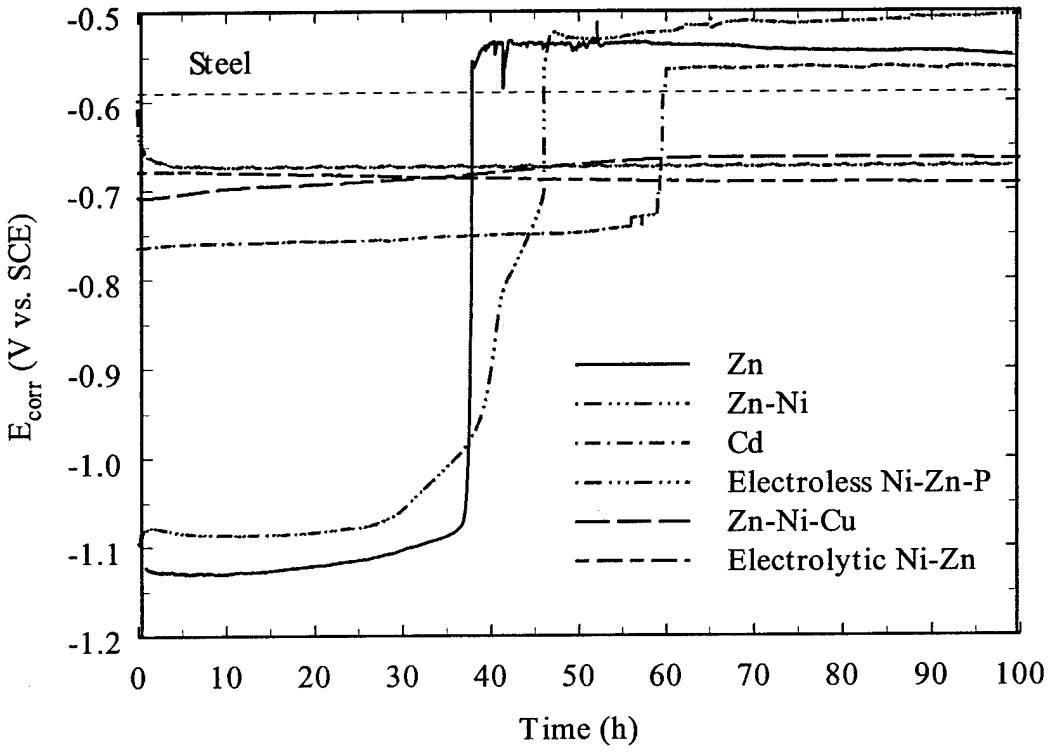

Figure 32 : E_{orr} vs. time plot for the various alloy coatings (thickness=2 μm) immersed in 71 g/L Na_2SO_4 and 30.5 g/L H_3BO_3 (pH=7.0).

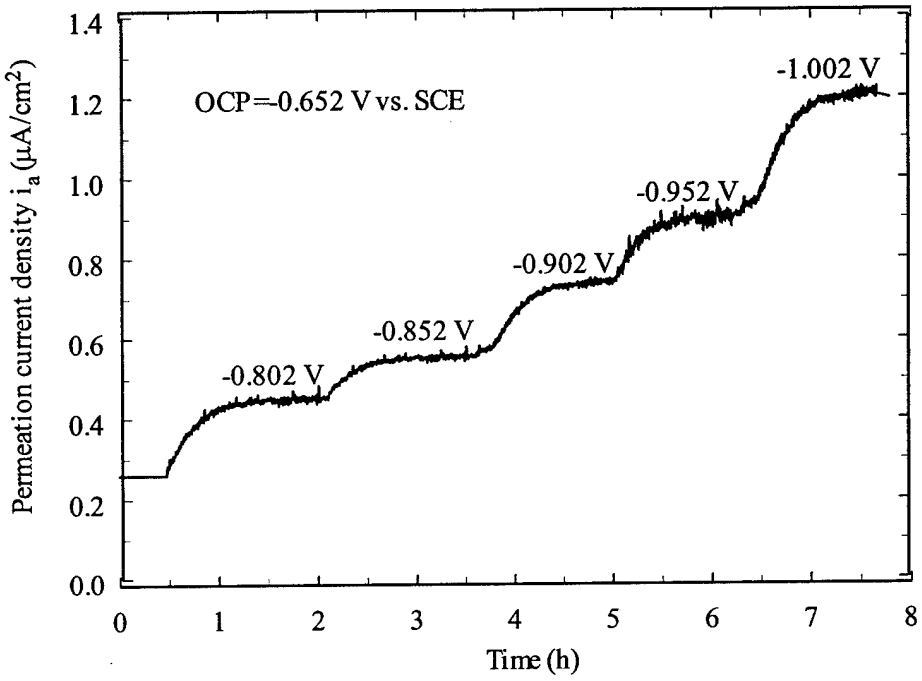

Figure 33: Hydrogen permeation current transients through Ni-Zn-P deposit as a function of time for different applied cathodic potentials.

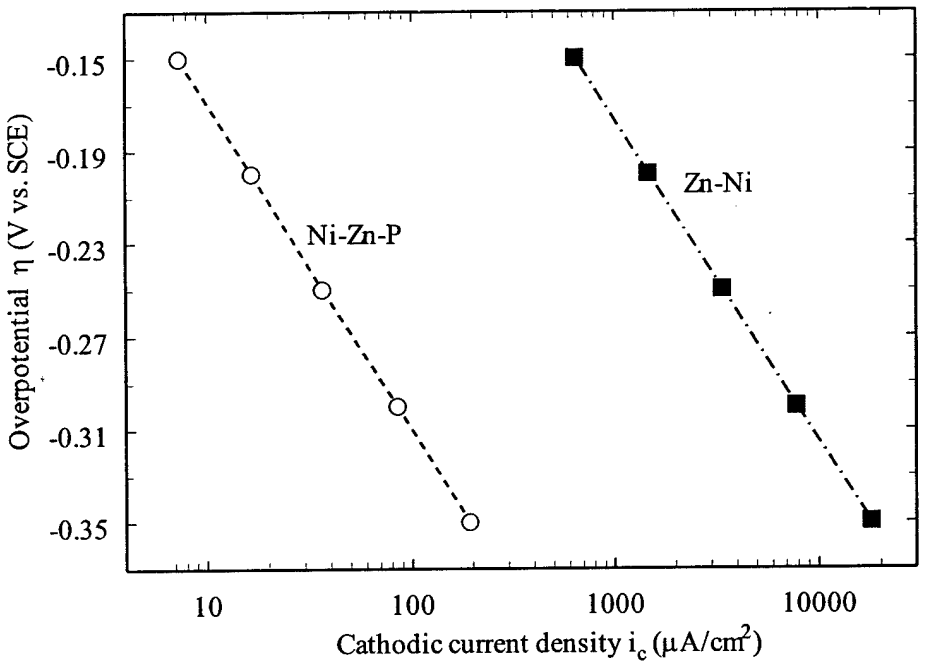

Figure 34: Variation of cathodic current densities (i_c) as a function of applied overpotential (η) for Ni-Zn-P and Zn-Ni deposits.

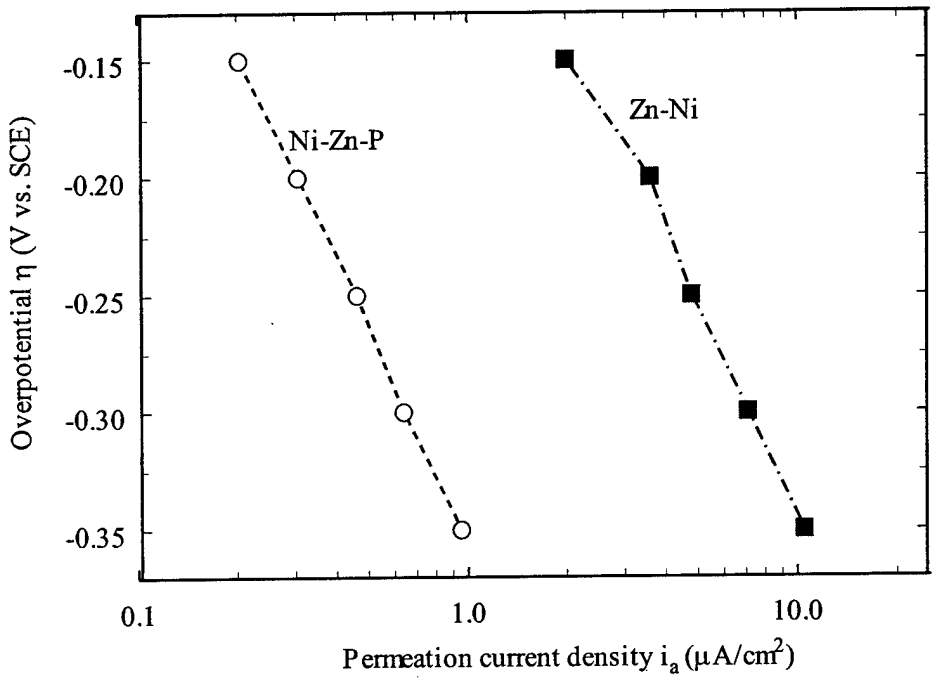

Figure 35: Variation of hydrogen permeation current densities (i_a) as a function of applied overpotential (η) for Ni-Zn-P and Zn-Ni deposits

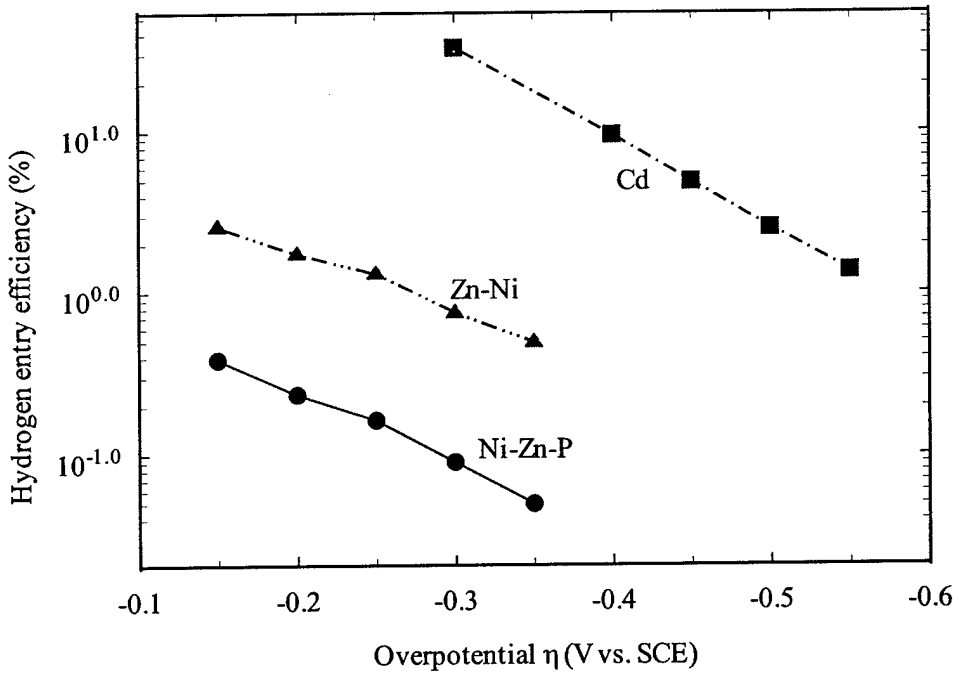

.Figure 36: The hydrogen entry efficiency (i_a/i_c x 100) as a function of overpotential (η) for Zn-Ni, Ni-Zn-P and Cd coatings.

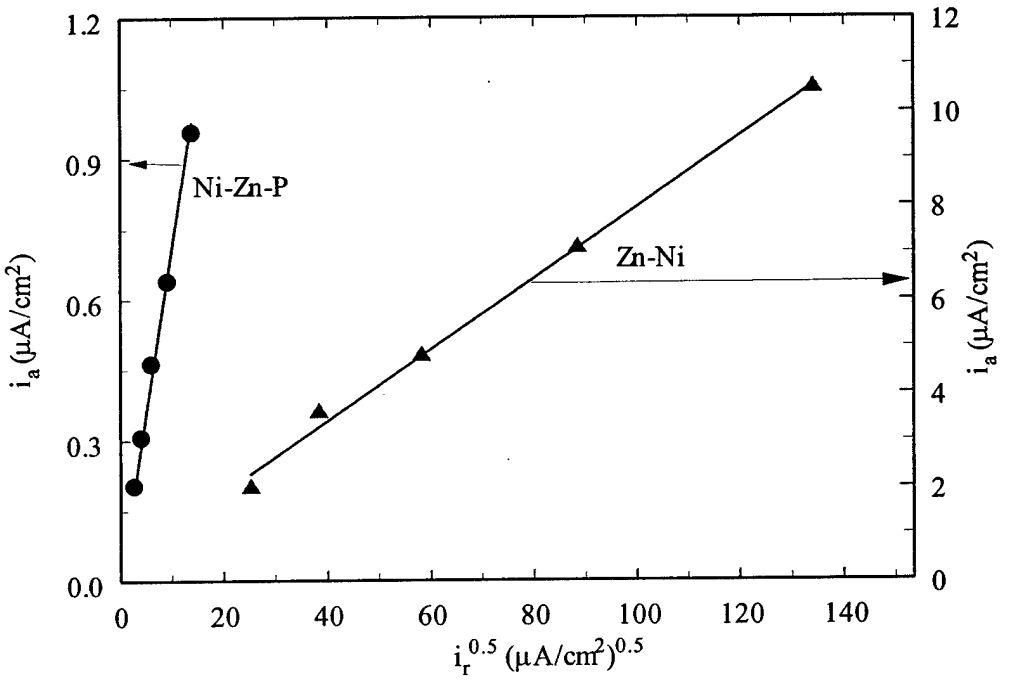

Figure 37: Plot of hydrogen permeation current (i_a) vs. square root of the recombination current ($\sqrt{i_r}$) for Ni-Zn-P and Zn-Ni coatings.

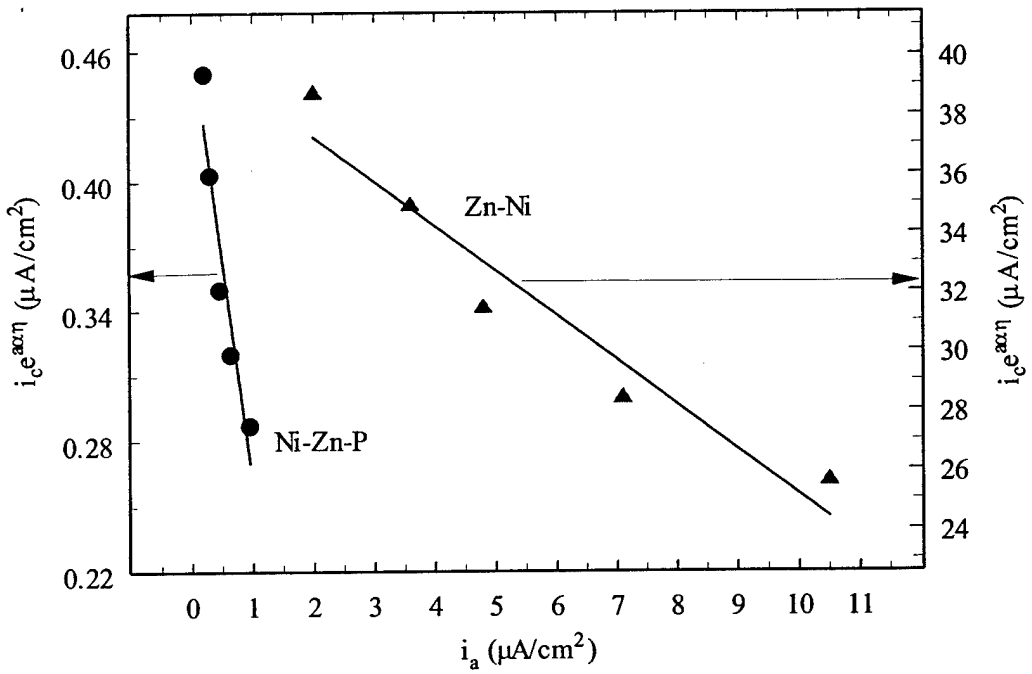

Figure 38: Plot of hydrogen charging function ($i_c e^{a\alpha\eta}$) vs. steady state hydrogen permeation current (i_a) for Ni-Zn-P and Zn-Ni coating

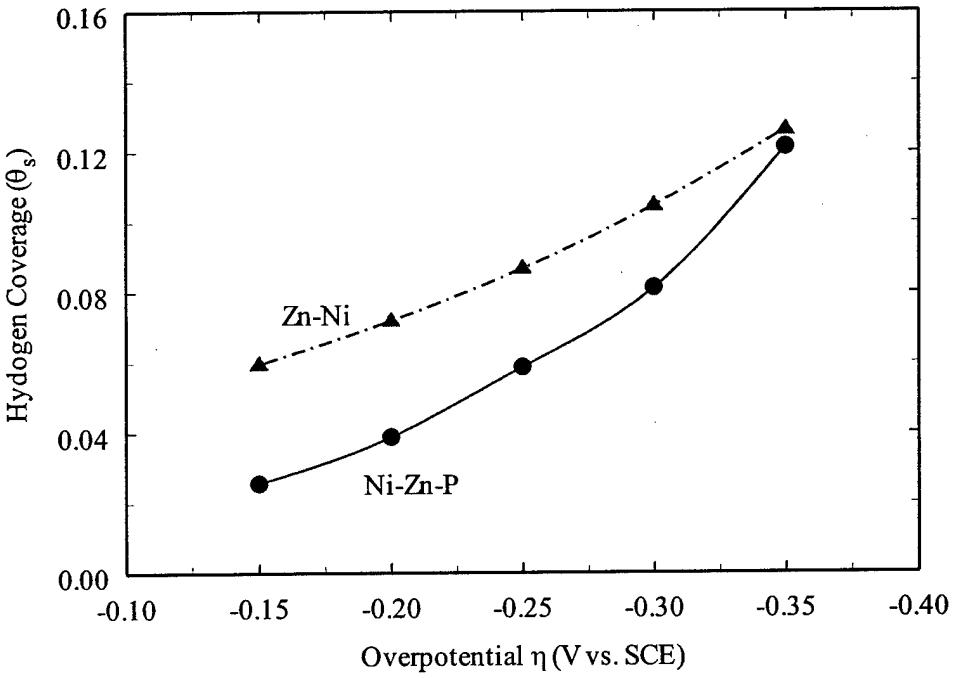

Figure 39: Dependence of surface hydrogen coverage (θ_s) on the hydrogen overpotential (η) for Ni-Zn-P, and Zn-Ni coatings.